

# Thermodynamic and Kinematic Influences on Precipitation Symmetry in Sheared Tropical Cyclones: Bertha and Cristobal (2014)

LEON T. NGUYEN, ROBERT F. ROGERS, AND PAUL D. REASOR

*NOAA/Atlantic Oceanographic and Meteorological Laboratory/Hurricane Research Division, Miami, Florida*

(Manuscript received 23 March 2017, in final form 11 August 2017)

## ABSTRACT

Prior studies have shown an association between symmetrically distributed precipitation and tropical cyclone (TC) intensification. Although environmental vertical wind shear typically forces an asymmetric precipitation distribution in TCs, the magnitude of this asymmetry can exhibit considerable variability, even among TCs that experience similar shear magnitudes. This observational study examines the thermodynamic and kinematic influences on precipitation symmetry in two such cases: Bertha and Cristobal (2014). Consistent with the impact of the shear, both TCs exhibited a tilted vortex as well as a pronounced azimuthal asymmetry, with the maximum precipitation occurring in the downshear-left quadrant. However, Bertha was characterized by more symmetrically distributed precipitation and relatively modest vertical motions, while Cristobal was characterized by more azimuthally confined precipitation and much more vigorous vertical motions. Observations showed three potential hindrances to precipitation symmetry that were more prevalent in Cristobal than in Bertha: (i) convective downdrafts that transported low entropy air downward into the boundary layer, cooling and stabilizing the lower troposphere downstream in the left-of-shear and upshear quadrants; (ii) subsidence in the upshear quadrants, which acted to increase the temperature and decrease the relative humidity of the midtroposphere, resulting in capping of the boundary layer; and (iii) lateral advection of midtropospheric dry air from the environment, which dried the TC's upshear quadrants.

## 1. Introduction

Although tropical cyclone (TC) intensity forecasts have shown statistically significant improvement during the past couple decades (DeMaria et al. 2014), further improvements remain a significant challenge. Many observational studies have shown that environmental vertical wind shear has a negative influence on TC intensity change (e.g., DeMaria and Kaplan 1994; Kaplan and DeMaria 2003; Kaplan et al. 2010). Recent idealized modeling studies have shown that the predictability of TC intensity change decreases with increasing environmental shear, at least up to a threshold shear magnitude beyond which the simulated TC does not intensify (Zhang and Tao 2013; Tao and Zhang 2015). These results highlight the need to improve our physical understanding of how tropical cyclones respond to environmental shear.

Environmental vertical wind shear can negatively affect TC intensity through several possible mechanisms. Outward fluxes of potential vorticity and equivalent

potential temperature can result in the weakening of the upper-level warm core, as proposed by Frank and Ritchie (2001). Midlevel ventilation, which is the intrusion of near-environmental dry air into the TC inner core, has been hypothesized to be another mechanism by which TCs can weaken in shear (Simpson and Riehl 1958; Tang and Emanuel 2010). Shear can also affect TC intensity through downdrafts that transport low entropy air from the midtroposphere down into the boundary layer (Barnes et al. 1983; Powell 1990; Riemer et al. 2010, 2013; Tang and Emanuel 2010). In Riemer et al.'s (2010, 2013) idealized simulations of shear interacting with a mature TC, downdrafts associated with an asymmetric convective band outside the eyewall deposited low entropy air into the inflow layer. This low entropy inflow air reached the eyewall, resulting in a decrease in the eyewall mean entropy and the TC's intensity (Riemer and Laliberté 2015).

The tilting of the TC vortex by the environmental shear can play a role in these weakening mechanisms; for example, by exciting eddies that mix midtropospheric low entropy air into the inner core (e.g., Tang and Emanuel 2012), or through forcing the asymmetric

---

*Corresponding author:* Leon T. Nguyen, leon.nguyen@noaa.gov

DOI: 10.1175/MWR-D-17-0073.1

© 2017 American Meteorological Society. For information regarding reuse of this content and general copyright information, consult the AMS Copyright Policy ([www.ametsoc.org/PUBSReuseLicenses](http://www.ametsoc.org/PUBSReuseLicenses)).

convective band and associated downdrafts that lead to a decrease in the eyewall mean entropy (Riemer et al. 2010, 2013). As a result, how TCs can reduce their tilt amid environmental shear has received much attention in the literature. In Jones's (1995) simulations using a hydrostatic, dry, primitive equation model, the vertical projection of the tilted PV anomaly resulted in precession of the vortex. If the vortex is able to precess upshear, the shear can help restore the vortex back to vertical alignment, as shown by recent simulations by Finocchio et al. (2016). Others have approached the issue of vortex alignment through the perspective of vortex Rossby wave (VRW) damping (e.g., Reasor and Montgomery 2001; Schecter et al. 2002; Reasor et al. 2004). In this view, the vortex tilt can be viewed as an asymmetric perturbation that projects onto VRWs, and their subsequent damping leads to a reduction of the tilt. Diabatic heating can help the TC vortex reduce its tilt in several ways: by increasing the precession frequency through reduced static stability (Jones 1995); by increasing the radial PV gradient and reducing the Rossby radius of deformation, which reduces the critical radius and increases the azimuthal propagation speed of the tilt mode (Reasor et al. 2004; Schecter and Montgomery 2007; Reasor and Montgomery 2015); or by helping to develop a new vortex through vortex stretching, a process known as downshear reformation (Molinari et al. 2004; Molinari and Vollaro 2010; Nguyen and Molinari 2015).

The interaction of environmental vertical wind shear with tropical cyclones results in an azimuthal asymmetry in convection and precipitation, as shown by various observational studies (e.g., Corbosiero and Molinari 2002; Chen et al. 2006; Reasor et al. 2013). There are several proposed mechanisms for this asymmetry. In Jones's (1995) dry simulations, the vortex was tilted because of the imposed environmental shear, and a balanced negative (positive) potential temperature perturbation initially developed on the downtilt (uptilt) side, as required for a balanced vortex. The cyclonic flow associated with the vortex then interacted with the downtilt cold anomaly, resulting in isentropic lift and maximum vertical motion located approximately  $90^\circ$  to the right of the tilt direction. In contrast, later simulations that include moist physics show a maximum in vertical motion nearly collocated with the tilt direction (Braun et al. 2006; Wu et al. 2006; Davis et al. 2008), and airborne Doppler radar composites appear to support this as well (Reasor et al. 2013). Another proposed explanation for the azimuthal vertical motion asymmetry is that low-level convergence develops downshear because of the tendency for vortex stretching to balance the radial advection of vorticity by the TC-relative

asymmetric flow (Willoughby et al. 1984; Bender 1997; Frank and Ritchie 2001). A third explanation for the asymmetry involves frictional convergence produced by asymmetric vorticity anomalies within the boundary layer tied to the vortex tilt (Riemer et al. 2010, 2013).

Observational studies have also shown that the magnitude of the precipitation or vertical motion asymmetry generally increases as the shear increases. This can lead to a decrease in the projection of diabatic heating onto the axisymmetric, azimuthal wavenumber-0 component that has been shown to be important for TC intensification in idealized simulations (e.g., Nolan and Grasso 2003; Nolan et al. 2007). Observational studies using passive microwave satellite (Kieper and Jiang 2012; Zagrodnik and Jiang 2014; Tao and Jiang 2015; Alvey et al. 2015) and airborne Doppler radar data (Rogers et al. 2013) have shown that rapidly intensifying TCs typically have a more symmetric precipitation distribution than slowly intensifying, steady-state, or weakening TCs. Thus, the development of a more symmetric precipitation and diabatic heating distribution appears to be crucial to the intensification of sheared TCs.

Recently, several hypotheses have been proposed to explain precipitation and diabatic heating symmetry differences among sheared TCs. One hypothesis is the azimuthal distribution of boundary layer moist entropy. In their idealized simulations, Rappin and Nolan (2012) found that when the surface environmental flow was oriented opposite of the shear vector (counteraligned), the simulated TCs were able to intensify, but when the surface environmental flow was oriented parallel to the shear vector (aligned), the simulated TCs did not intensify. In the counteraligned configuration, the enhanced surface winds and enthalpy fluxes left of shear were able to replenish heat and moisture to the downdraft-cooled air more quickly, enabling the convection to propagate into the upshear quadrants. Onderlinde and Nolan (2016) found a similar association between enhanced surface enthalpy fluxes left of shear and a symmetric precipitation distribution when the TC-relative environmental helicity was positive.

Asymmetries in the midtropospheric moisture distribution can also influence precipitation and diabatic heating symmetry. In recent studies of Hurricane Edouard (2014), Zawislak et al. (2016) and Rogers et al. (2016) found that as Edouard intensified, the midlevels in the upshear quadrants progressively moistened. They hypothesized that this moistening reduced dry air entrainment into updrafts, enabling the convection to propagate into the upshear quadrants. In an idealized modeling study, Ge et al. (2013) found that midtropospheric dry air initially placed in the downshear-right

quadrant was advected cyclonically into the downshear side, suppressing convective activity there and preventing the developing tropical cyclone from becoming vertically aligned.

This study focuses on two Atlantic tropical cyclones during August 2014, Bertha and Cristobal, which differed substantially in the degree of precipitation symmetry despite both experiencing about  $10 \text{ m s}^{-1}$  of northwesterly to northerly environmental vertical wind shear. The reasons behind these symmetry differences are explored in particular detail. Both of these storms were sampled by several aircraft during their lifetimes, including the National Oceanic and Atmospheric Administration (NOAA) WP-3D (P-3), Gulfstream-IV (G-IV), and the Air Force Reserve (AFR) C-130. The paper will be organized as follows. [Section 2](#) discusses the data and methods used. [Section 3](#) gives a broad, synoptic-scale overview of the two cases. An overview of the precipitation structure, vortex tilt, and the intensity of convection in both storms is provided in [section 4](#). The observed thermodynamic asymmetries and their potential impacts on the asymmetric precipitation structure of both storms are discussed in [section 5](#). [Section 6](#) summarizes the results and presents potential avenues for future research.

## 2. Data and methods

Much of the data used in this study were obtained from aircraft missions. The four NOAA (three P-3, one G-IV) flights into Bertha encompass the rapid intensification (RI), the end of RI, and the beginning of the weakening period. There were nine NOAA (seven P-3, two G-IV) flights into Cristobal during its slow intensification and steady-state periods.

Three-dimensional analyses of reflectivity and winds from the P-3 and G-IV airborne X-band tail Doppler radar (TDR) were used in this study. These three-dimensional analyses have horizontal and vertical spacing of 2 and 0.5 km, respectively. To produce these analyses, an automated variational algorithm that simultaneously solves the Doppler radar projection and mass continuity equations was applied to the measured reflectivity and radial velocity ([Gamache 1997](#); [Reasor et al. 2009](#)). The P-3 TDR analyses are produced for each radial pass through the storm, encompassing  $\sim 1.5 \text{ h}$  in time. The G-IV TDR analyses are produced for the two innermost circles around the storm, encompassing  $\sim 2.5 \text{ h}$  in time. Many recent studies have used P-3 TDR analyses derived using this variational algorithm (e.g., [Reasor et al. 2013](#); [Rogers et al. 2013, 2015, 2016](#)), but to our knowledge this is the first study that has used G-IV TDR analyses since it became operational in 2012. The differences between the P-3

TDR and G-IV TDR will be summarized briefly as follows. As with the P-3, the G-IV employs a fore–aft scanning technique in which the antenna scans  $20^\circ$  fore and aft of the plane normal to the fuselage. However, the G-IV has a greater ground speed ( $\sim 230 \text{ m s}^{-1}$ ) than the P-3 ( $\sim 140 \text{ m s}^{-1}$ ), resulting in coarser spatial sampling. To mitigate this, the G-IV uses a dual transmitter–receiver system in which the fore and aft beams scan simultaneously, instead of alternately as the P-3 currently does. This enables the typical along-track spacing between the fore and aft beam crossings to be similar between the P-3 (1.7 km) and G-IV (1.4 km) radars. The G-IV TDR has been shown to perform as well as the P-3 TDR in an operational systems acceptance test and in intercomparisons within several tropical cyclones ([Reasor et al. 2016](#)).

Dropsondes provide high vertical resolution profiles of atmospheric pressure, temperature, humidity, wind speed, and wind direction as they descend from flight level ([Hock and Franklin 1999](#)). All dropsondes were postprocessed using the National Center for Atmospheric Research’s (NCAR) Atmospheric Sounding Process Environment (ASPEN) software. Dropsondes with erroneous saturated, near dry-adiabatic layers near the surface (8% of those used in this study) were corrected following [Bogner et al. \(2000\)](#). The dropsonde locations were transformed into TC-relative coordinates as follows: the average latitude–longitude of each dropsonde profile was used to compute the position relative to the flight-level wind center positions (at 2-min time resolution) derived from the methodology of [Willoughby and Chelmon \(1982\)](#). The TC-relative winds were calculated by removing the 6-hourly TC motion centered on the dropsonde or TDR analysis time.

Polarization-corrected temperatures (PCT) were computed from Special Sensor Microwave Imager/Sounder (SSMIS) data. Sea surface temperatures (SSTs) were obtained from the NOAA  $\frac{1}{4}^\circ$  resolution daily SST dataset ([Reynolds et al. 2007](#)), which incorporates the Advanced Very High Resolution Radiometer (AVHRR) infrared satellite data, the Advanced Microwave Scanning Radiometer (AMSR) data, as well as SST data from ships and buoys. The environmental wind was computed from  $0.5^\circ$  Global Forecast System (GFS) analyses following the methodology of [Galarneau and Davis \(2013\)](#). The divergent and rotational winds associated with the TC vortex were subtracted from the total wind out to a radius of 500 km, and the remaining environmental wind field was averaged within a circle of radius of 500 km at specified vertical levels. The 850–200 hPa shear vector was computed by taking the difference between the mean 850- and 200-hPa environmental winds within 500-km radius.

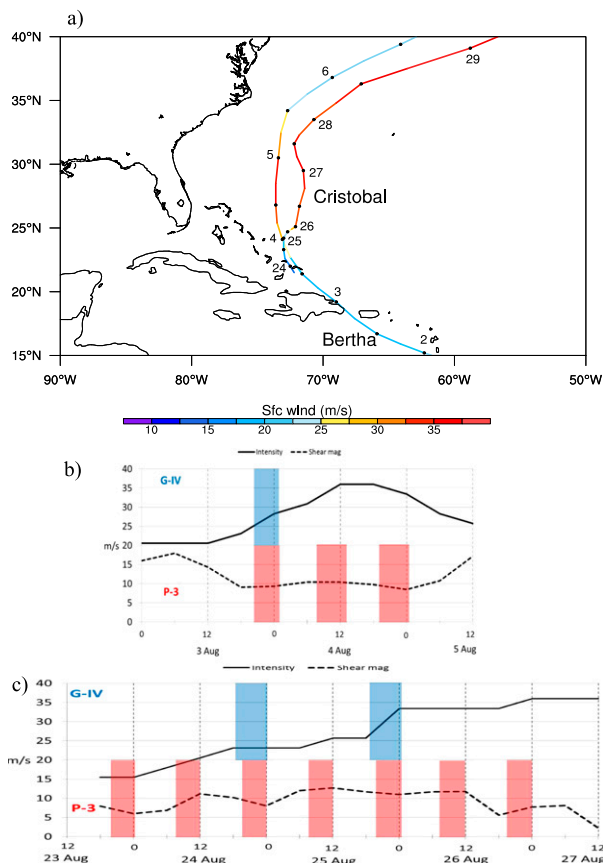


FIG. 1. (a) Best track position and intensity ( $\text{m s}^{-1}$ ) of Bertha and Cristobal. Intensity (solid) and environmental vertical wind shear (dashed) for (b) Bertha and (c) Cristobal. Approximate on-station times of P-3 (red bars) and G-IV (blue bars) are indicated.

### 3. Overview of cases

Bertha originated from an African easterly wave and was declared a tropical storm at 0000 UTC 1 August about 500 km east of the Lesser Antilles (Blake 2015). After passing north of Puerto Rico and Hispaniola (Fig. 1a), Bertha intensified from 40 to 70 kt ( $20.6\text{--}36.0 \text{ m s}^{-1}$ ) between 1200 UTC 3 August and 1200 UTC 4 August (Fig. 1b), meeting the  $30 \text{ kt } (24 \text{ h})^{-1}$  criterion for rapid intensification (Kaplan et al. 2010). Analyzed sea surface temperatures were approximately  $28\text{--}29^\circ\text{C}$  during this period (Figs. 2a,b). The southerly to southeasterly low-level flow due to the low-level ridge to the northeast (Fig. 3e) and the weakened upper-level flow due to the upper-level trough to the north (Fig. 3a) resulted in the  $10 \text{ m s}^{-1}$  of north-northwesterly 850–200-hPa environmental vertical wind shear (Fig. 1b). After reaching a peak intensity of 70 kt ( $36 \text{ m s}^{-1}$ ) at 1200 UTC 4 August, Bertha leveled off in intensity, began to weaken at 1800 UTC 4 August, and continued to weaken as

the shear increased to over  $15 \text{ m s}^{-1}$  after 0600 UTC 5 August.

Cristobal also originated from an African easterly wave, but did not develop a well-defined circulation until 1800 UTC 23 August, when it was declared a tropical depression (Pasch 2015). Cristobal moved slowly north-eastward east of the Bahamas (Fig. 1a) and gradually intensified over the next couple days up to 65 kt ( $33.4 \text{ m s}^{-1}$ ) by 0000 UTC 26 August (Fig. 1c). Analyzed SSTs during the intensification period ranged from  $27^\circ$  to  $29^\circ\text{C}$  (Figs. 2d–f). The upper-level trough digging from the north (Figs. 3c,d) contributed to north-northwesterly upper-level environmental flow, and the low-level ridge to the east (Figs. 3g,h) contributed to south-southeasterly low-level environmental flow, yielding  $10\text{--}12 \text{ m s}^{-1}$  of north-northwesterly shear. Between 0000 UTC 26 August and 1200 UTC 27 August, Cristobal remained steady in intensity between 65 and 70 kt ( $33.4\text{--}36.0 \text{ m s}^{-1}$ ) despite decreasing environmental shear (Fig. 1c) and SSTs of  $28\text{--}29^\circ\text{C}$  (Fig. 2f). Cristobal encountered cooler SSTs of around  $27^\circ\text{C}$  on 27–28 August (not shown), but was able to maintain an intensity of 65–75 kt ( $33.4\text{--}38.6 \text{ m s}^{-1}$ ) until it was declared extratropical at 1200 UTC 29 August.

During both Bertha's and Cristobal's intensification and subsequent steady-state/weakening phases, the 850–200-hPa environmental shear was consistently north-westerly to northerly at between  $9$  and  $12 \text{ m s}^{-1}$  (Figs. 1b,c). Nevertheless, the vertical distribution of the shear showed discernable differences between the two cases. Figure 4 shows hodographs of the environmental wind averaged within the 500-km radius of Bertha and Cristobal, as well as the cumulative hodograph length during their respective periods of interest. The cumulative hodograph length was found by computing the shear magnitude between adjacent interpolated (200-m vertical resolution) vertical levels, and then integrating upward starting from 1.5-km altitude (approximately 850-hPa pressure level). This provides a measure of how “bottom heavy” the environmental vertical wind shear profile is. Finocchio and Majumdar (2017) used a similar methodology in their climatology of TC environmental wind profiles. The mean cumulative hodograph lengths of the two cases were similar below 4-km altitude, but diverged above that altitude until about 7-km altitude, above which the difference remained approximately constant. This indicates that Cristobal was experiencing greater shear in the 4–7-km vertical layer than Bertha. In a recent study, Finocchio et al. (2016) showed that in their idealized simulations, lower-level shear was more destructive than upper-level shear because it encouraged intrusions of midlevel dry air into the tropical cyclone inner core, which acted to invigorate convective downdrafts that transported low entropy air into the boundary



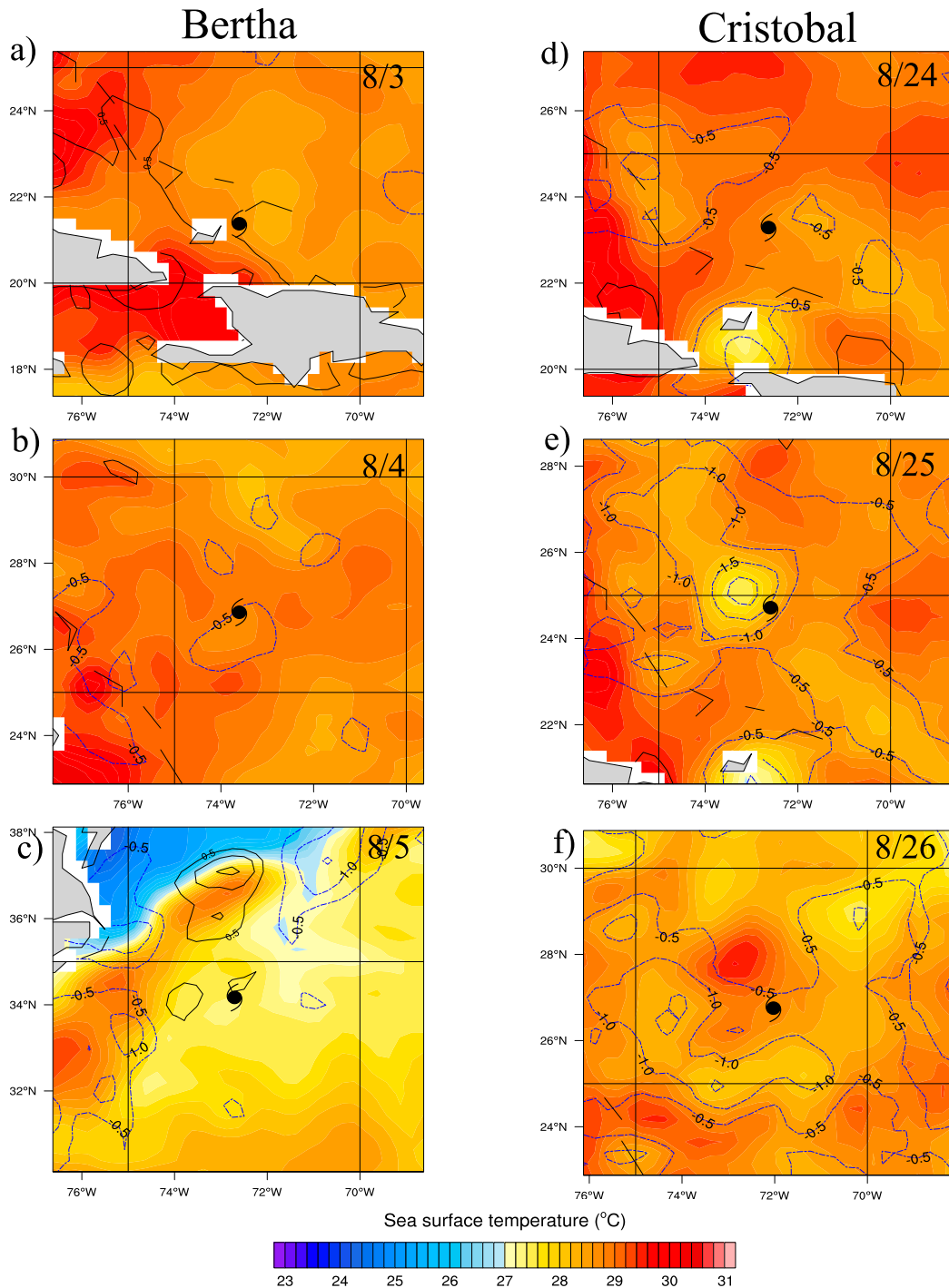


FIG. 2. Sea surface temperatures (shaded, °C) centered on the daily 1200 UTC best track position for (a)–(c) Bertha and (d)–(f) Cristobal. Line contours (solid black, positive; dashed blue, negative) indicate the SST difference from three days prior.

layer. Observational evidence of these processes will be shown in later sections of this paper.

The remainder of the paper will discuss the precipitation asymmetry, as well as the potential thermodynamic and

kinematic influences on that asymmetry in both storms. Particular focus will be on observations during the 1800 UTC 3 August–0000 UTC 4 August period in Bertha (Fig. 1b), and the 1800 UTC 25 August–0000 UTC

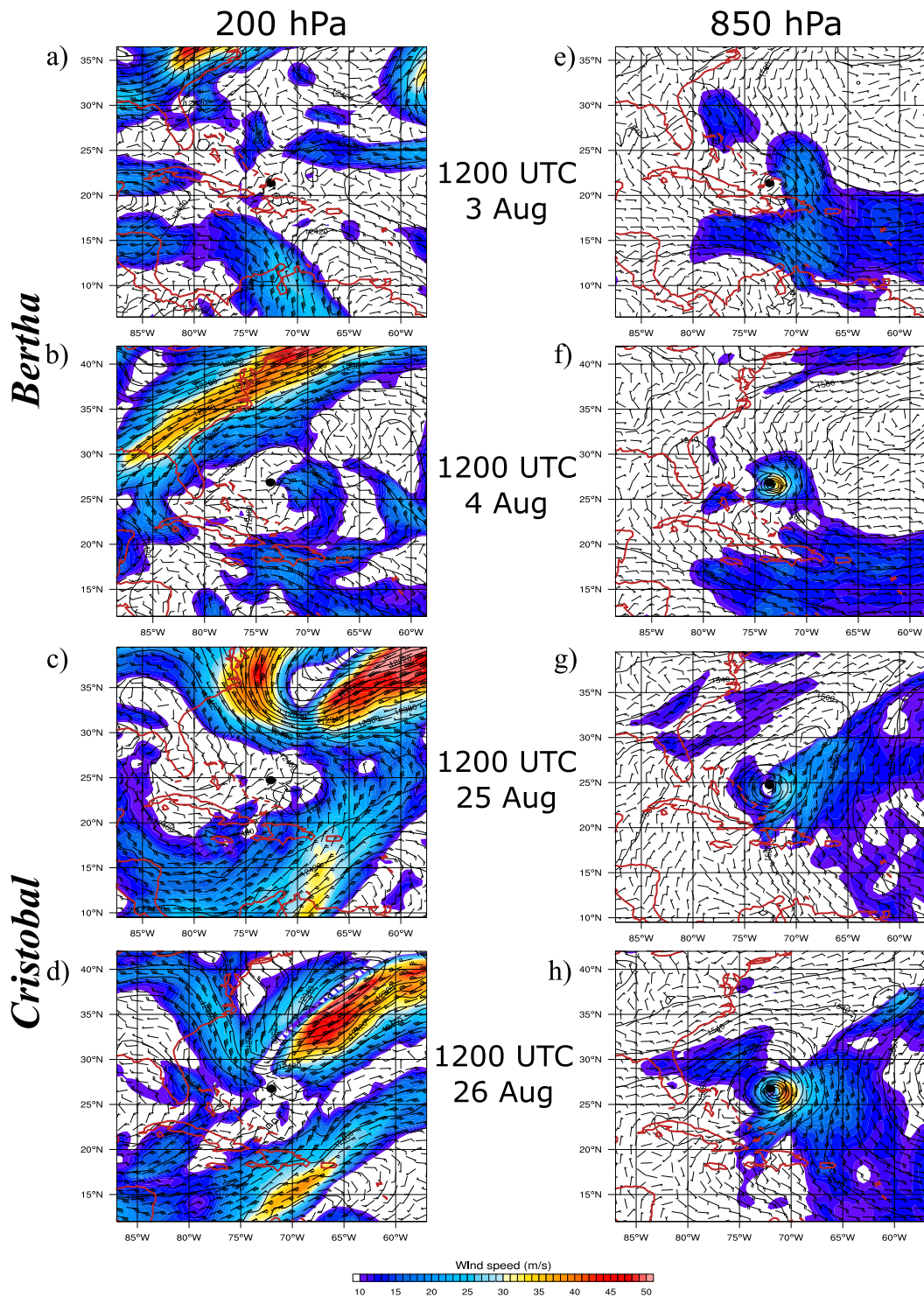


FIG. 3. (a)–(d) The 200-hPa and (e)–(h) 850-hPa wind speed (shaded,  $\text{m s}^{-1}$ ) and geopotential height (contours) for (a), (b), (e), (f) Bertha and (c), (d), (g), (h) Cristobal. Images are centered on the TC center.

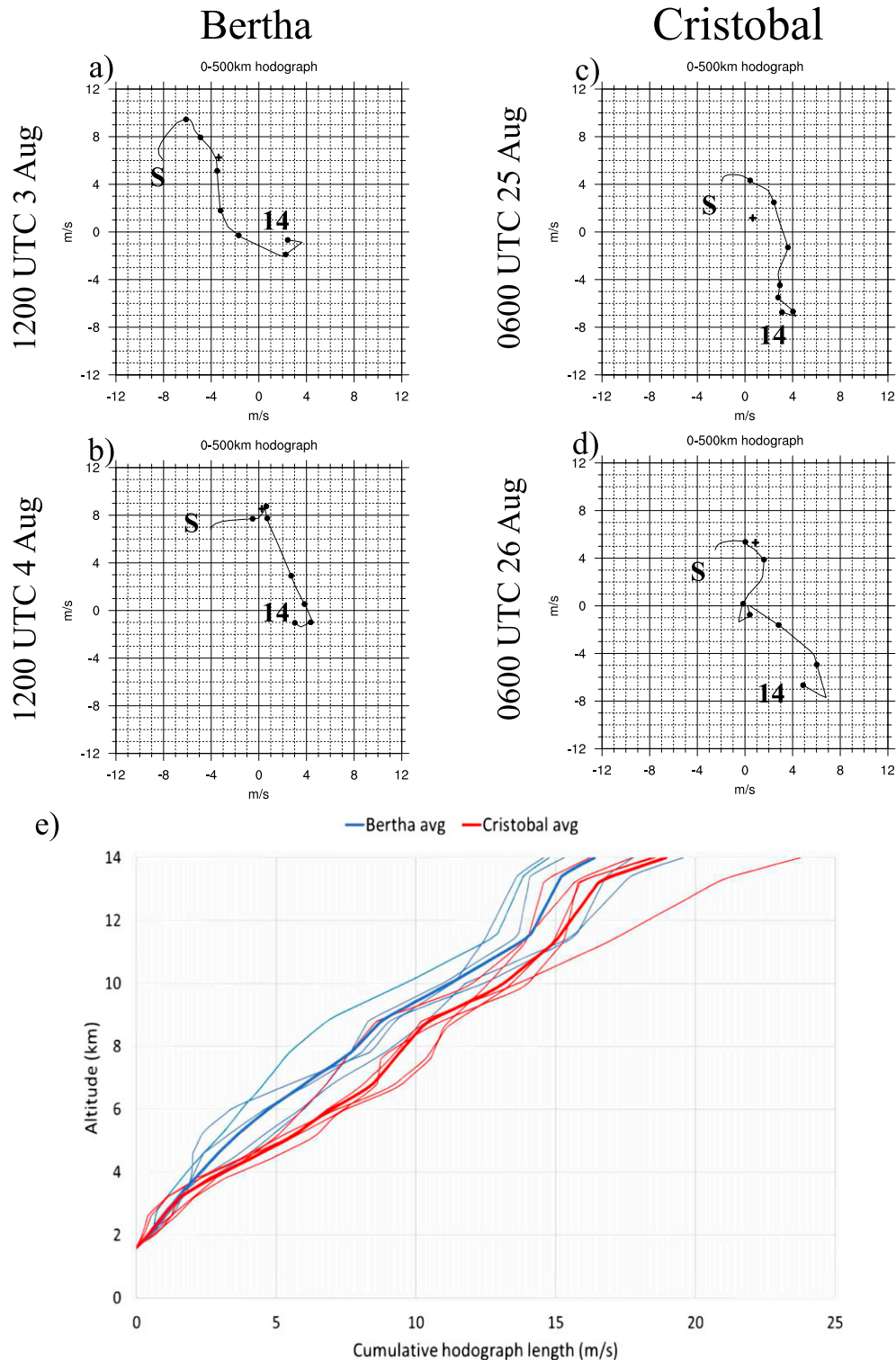


FIG. 4. Hodographs of the environmental wind averaged within the 500-km radius for (a),(b) Bertha and (c),(d) Cristobal, with the vortex removed following the method of [Galarneau and Davis \(2013\)](#). Each dot represents a 2-km height increment, starting from the surface (denoted by “S”) and ending at 14-km height (denoted by “14”). Small cross denotes the storm motion. (e) Cumulative hodograph length for Bertha and Cristobal. Thick lines denote the mean, and thin lines denote individual times within the averaging period (1200 UTC 3 Aug–1200 UTC 4 Aug for Bertha, 0600 UTC 25 Aug–0600 UTC 26 Aug for Cristobal).

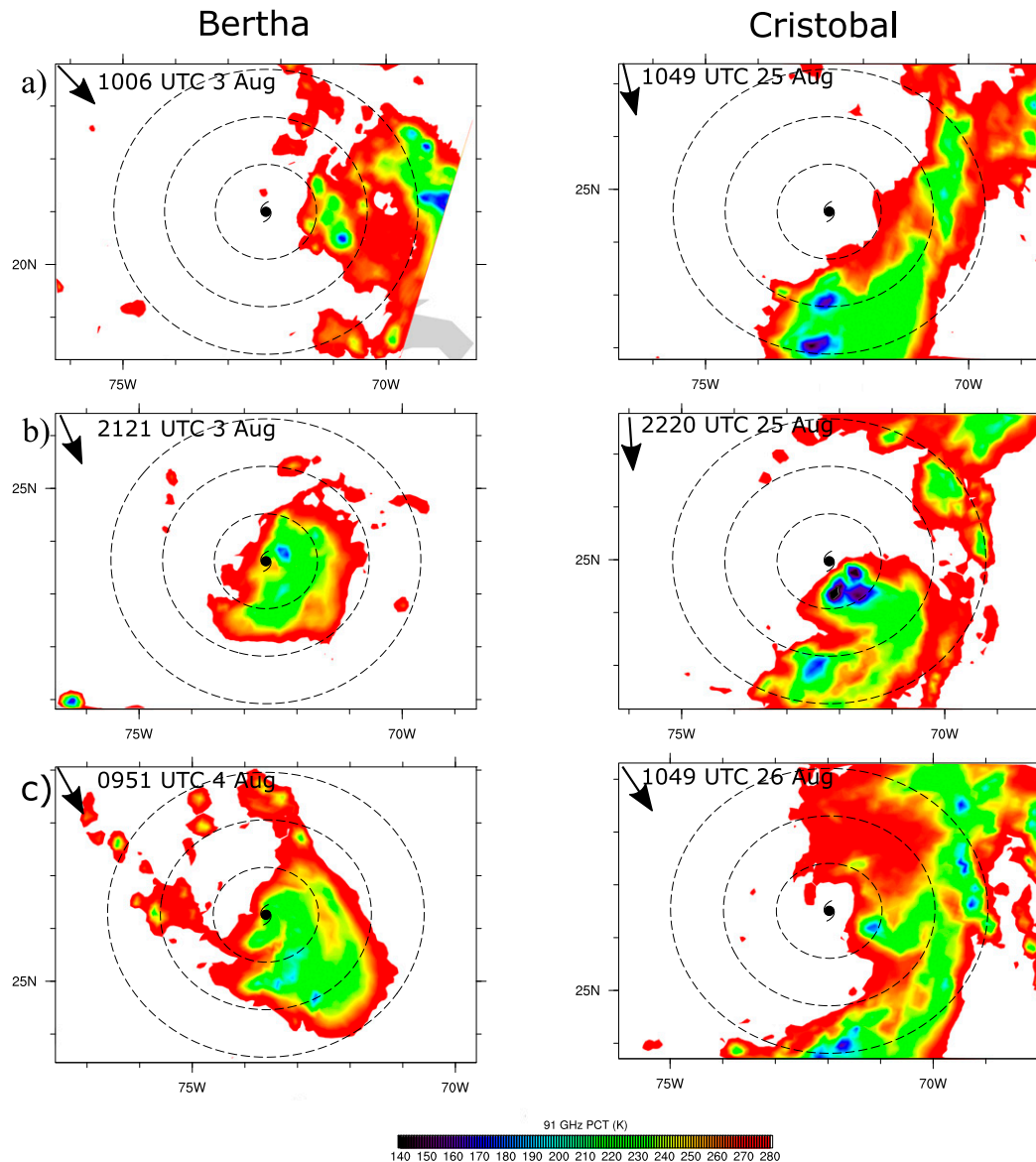


FIG. 5. The 91.7-GHz polarization-corrected temperature (PCT) from passive microwave overpasses of Bertha at (a) 1006 UTC 3 Aug, (b) 2121 UTC 3 Aug, and (c) 0951 UTC 4 Aug; and of Cristobal at (d) 1103 UTC 25 Aug, (e) 2220 UTC 25 Aug, and (f) 1049 UTC 26 Aug. Shear vector is shown at top left of each panel. Range rings are every 100 km.

26 August period in Cristobal (Fig. 1c). During these periods, both the P-3 and G-IV aircraft were flying in or near these storms, enabling the kinematic and thermodynamic structure to be assessed throughout the troposphere.

#### 4. Precipitation/convective structure and vortex tilt

##### a. Precipitation and radial flow asymmetry

The interaction of environmental shear with the TC vortex resulted in a pronounced azimuthal asymmetry in precipitation in both Bertha and Cristobal. Figure 5

shows the PCT from a sequence of passive microwave overpasses spanning the RI period of Bertha (3–4 August) and near the end of the slow intensification period of Cristobal (25–26 August). Both storms exhibited a strong precipitation asymmetry, with precipitation maximized in the downshear-left quadrant and minimized in the upshear quadrants. The azimuthal asymmetry in precipitation was consistent with airborne radar (e.g., Rogers et al. 2013; Reasor et al. 2013) and microwave (e.g., Chen et al. 2006; Alvey et al. 2015; Tao and Jiang 2015) composite studies of tropical cyclones in



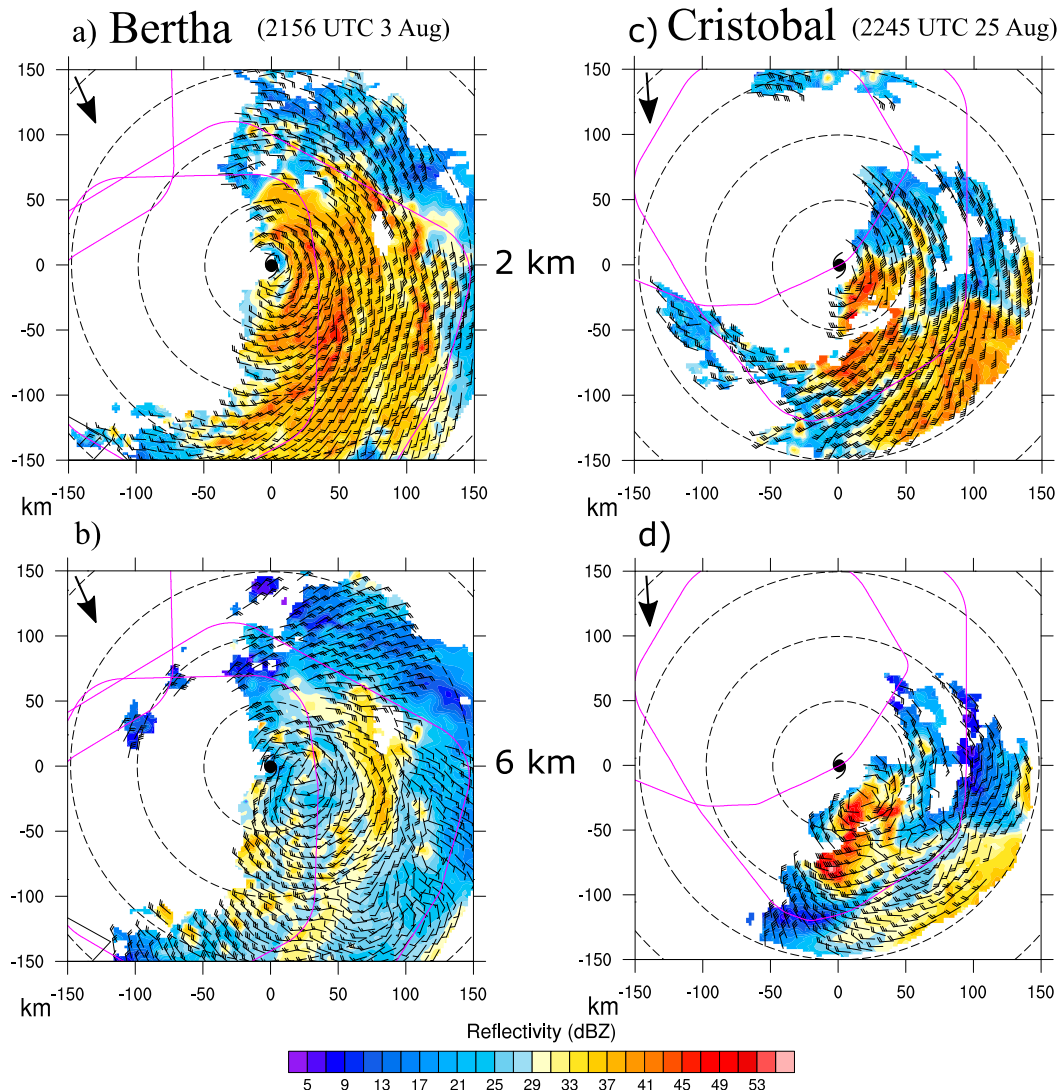


FIG. 6. Reflectivity (shaded, dBZ) and TC-relative winds derived from the G-IV tail Doppler radar in Bertha for the analysis centered at 2156 UTC 3 Aug at (a) 2- and (b) 6-km altitude; and in Cristobal for the analysis centered at 2245 UTC 25 Aug at (c) 2- and (d) 6-km altitude. The magenta line denotes the G-IV flight path. The subjectively determined circulation center at 2-km altitude is shown by the tropical cyclone symbol, and the environmental shear vector is shown at the top left. Range rings are every 50 km.

shear. Note that prior to RI onset, Bertha's precipitation was azimuthally confined to the downshear-left quadrant (Fig. 5a), but as RI progressed, the azimuthal coverage in precipitation increased, and the precipitation occurred closer to the TC center (Figs. 5b,c). In contrast, Cristobal's precipitation did not evolve toward increasing symmetry during this period (Figs. 5d-f).

Figure 6 shows reflectivity and TC-relative winds derived from the G-IV TDR centered at 2156 UTC 3 August in Bertha and 2245 UTC 25 August in Cristobal (concurrent with Figs. 5b and 5e). Although the TDR data coverage was insufficient to objectively determine the vortex tilt (e.g., Marks et al. 1992; Reasor et al. 2013),

qualitatively both storms showed a vortex tilt in the DSL direction. In Bertha, the 6-km circulation center (Fig. 6b) was displaced about 30–40 km to the east-southeast of the 2-km circulation center (Fig. 6a), while in Cristobal, the 6-km center (Fig. 6d) was displaced about 30–40 km to the southeast of the 2-km center (Fig. 6c). Bertha's 2–6-km tilt was reduced to about 15 km during the following P-3 mission 12 h later, while Cristobal's tilt during the P-3 mission 12 h later was indeterminable due to lack of reflectors. It could not be determined whether Bertha underwent vortex precession (e.g., Jones 1995; Finocchio et al. 2016) due to the 12-h spacing between observations of the vortex tilt. The observed downshear-left tilt in both storms



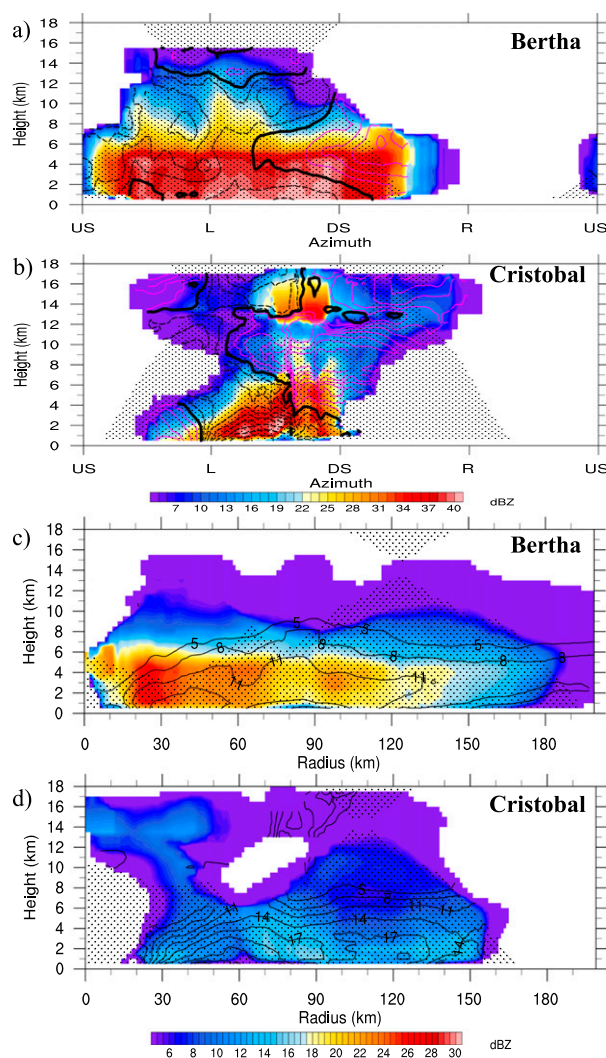


FIG. 7. (a) Azimuth–height plot of reflectivity (shaded, dBZ), TC-relative inflow (dashed black, contoured every 3 m s<sup>-1</sup> starting at -3 m s<sup>-1</sup>), and TC-relative outflow (solid magenta, contoured every 3 m s<sup>-1</sup> starting at 3 m s<sup>-1</sup>) averaged within 20–60-km radii for the 2156 UTC 3 Aug analysis in Bertha. Zero radial wind contour is bolded. “US,” “L,” “DS,” and “R” denote upshear, left of shear, downshear, and right of shear, respectively. (b) As in (a), but for the 2245 UTC Aug analysis in Cristobal. (c) Quasi-azimuthally averaged reflectivity (shaded, dBZ) and TC-relative tangential wind (contours, m s<sup>-1</sup>) shown for the 2156 UTC 3 Aug analysis in Bertha. (d) As in (c), but for the 2245 UTC 25 Aug analysis in Cristobal. Stippling in panels indicate >60% (a), (b) radial or (c), (d) azimuthal coverage by the G-IV TDR swath.

was broadly consistent with prior theoretical (Reasor et al. 2004), observational (e.g., Marks et al. 1992; Reasor et al. 2013), and modeling (e.g., Braun et al. 2006; Riemer et al. 2010) studies. The region of heaviest precipitation was located in the downtilt direction, also consistent with prior studies (e.g., Braun et al. 2006; Rogers et al. 2015).

Figures 7a and 7b show azimuth–height plots of reflectivity and TC-relative radial wind in both storms.

Note that Bertha’s precipitation at this time extended from the downshear right (DSR) cyclonically into the upshear-left (USL) quadrant (Fig. 7a), while Cristobal’s precipitation was mostly confined to the DSL quadrant (Fig. 7b). As a result, the azimuthal coverage of 2-km average reflectivity (within 20–60-km radii) exceeding 25 dBZ was 60% in Bertha compared to 25% in Cristobal. The enhanced USL precipitation in Bertha did not appear to be simply due to the advection of hydrometeors by TC-relative cyclonic flow, because the TC-relative cyclonic flow in Bertha’s USL quadrant ( $\sim 20 \text{ m s}^{-1}$  at 2-km altitude) was slightly weaker than in Cristobal’s ( $\sim 25 \text{ m s}^{-1}$  at 2-km altitude), as shown in Fig. 6. Although the concentric rings flown by the G-IV aircraft in both storms provided extensive azimuthal coverage, the G-IV did not sample the upshear-right (USR) quadrant within 50-km radius of Bertha and the USR quadrant of Cristobal. The concurrent passive microwave overpasses (Figs. 5b,d) generally confirm the lack of precipitation in these unsampled regions, however.

An azimuthal asymmetry in radial flow was also evident in both Bertha and Cristobal (Figs. 7a,b), with both storms exhibiting low-level inflow in the DSL quadrant, mid- to upper-tropospheric inflow in the USL quadrant, mid- to upper-tropospheric outflow in the DSR quadrant, and weakened low-level inflow in the USL quadrant. This pattern was qualitatively consistent with prior observational studies of sheared tropical cyclones (e.g., Reasor et al. 2013; Zhang et al. 2013; DeHart et al. 2014; Rogers et al. 2016). As with the precipitation asymmetry, there were clear differences in the magnitude of the radial flow asymmetry between the two storms. In the DSL quadrant, the low-level inflow was deeper and more intense in Cristobal, reaching near  $20 \text{ m s}^{-1}$  at 1-km altitude compared to  $6 \text{ m s}^{-1}$  inflow in Bertha. In the USL quadrant, low-level outflow of up to  $12 \text{ m s}^{-1}$  was observed in Cristobal, but the radial flow was weak in Bertha.

#### b. Quasi-azimuthally averaged reflectivity and radial location of heating

Figures 7c and 7d show the quasi-azimuthally averaged reflectivity and TC-relative winds derived from the G-IV TDR during the intensification of Bertha and Cristobal, respectively. Dataless grid points were included in the quasi-azimuthally averaged reflectivity by setting the reflectivity at these points equal to 0 dBZ, but were not included in the quasi-azimuthally averaged tangential wind because the winds were not zero in scatterer-free areas. It is important to note that these quantities do not represent true azimuthal averages because of the sampling gaps noted previously. To

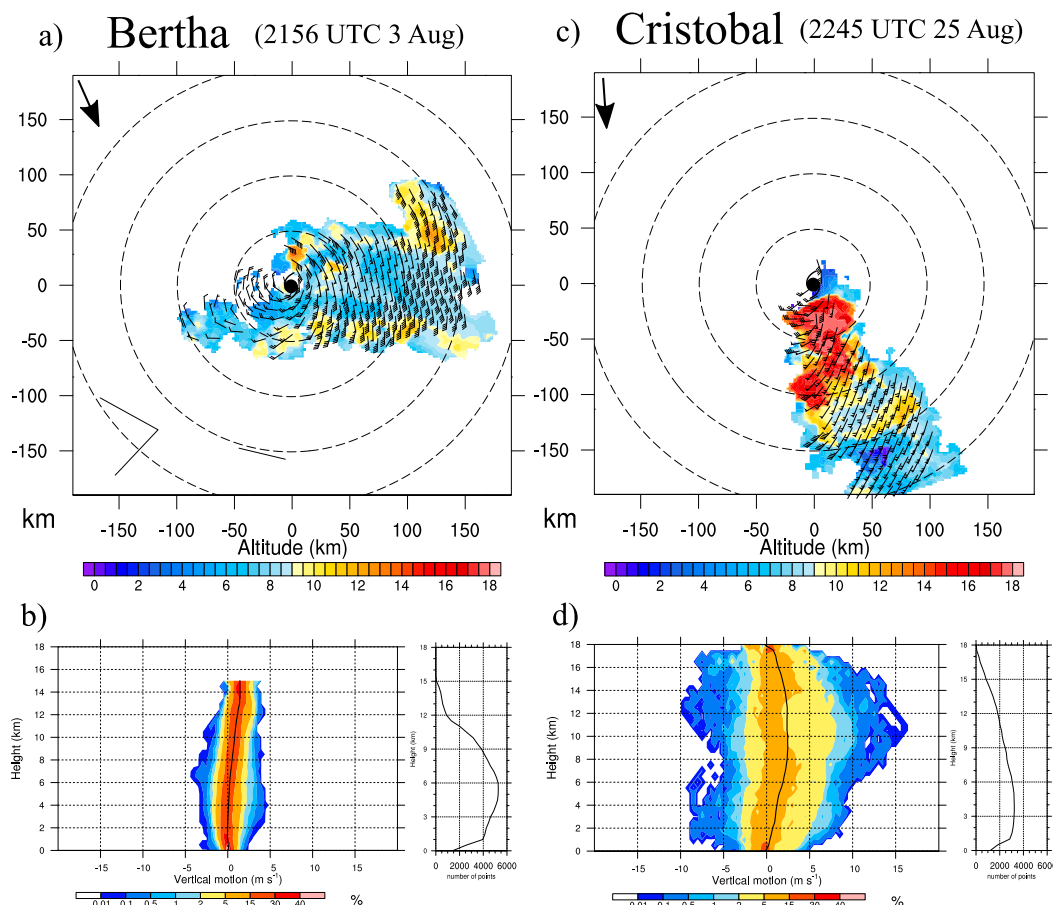


FIG. 8. (a) Height of the 20-dBZ echo top (shaded, km) and (b) CFAD of vertical velocity (shaded, %) derived from the P-3 tail Doppler radar during pass through Bertha centered at 2156 UTC 3 Aug. Mean vertical velocity denoted by solid black line. (c), (d) As in (a), (b), but for pass through Cristobal centered at 2328 UTC 25 Aug. TC-relative winds are overlain. Shear vector is shown at top left of (a) and (c). Range rings are every 50 km.

indicate these sampling gaps, stippling has been added to indicate where there was at least 60% azimuthal coverage by the TDR swath. Below 6-km altitude, Bertha's quasi-azimuthally averaged reflectivity was considerably higher than that of Cristobal at all radii. Bertha's larger quasi-azimuthally averaged reflectivity was consistent with a more-extensive azimuthal coverage of reflectivity, particularly in the USL quadrant.

The quasi-azimuthally averaged reflectivity within Bertha peaked at 26 dBZ at the 25-km radius, inside the radius of maximum wind (RMW). In contrast, the quasi-azimuthally averaged reflectivity within Cristobal peaked at only 17 dBZ at the 70-km radius, outside the RMW. Diabatic heating within the high inertial stability region inside the RMW (suggested by the peak reflectivity inside the RMW in Bertha) is a configuration shown to be favorable for TC intensification in idealized (e.g., Schubert and Hack 1982; Pendergrass and Willoughby 2009; Vigh and Schubert 2009) and

observational (e.g., Nguyen and Molinari 2012; Rogers et al. 2013; Stevenson et al. 2014; Rogers et al. 2015) studies. Schubert and Hack (1982) and Vigh and Schubert (2009) hypothesized that in the high inertial stability region, heat energy is more efficiently converted to kinetic energy. Alternatively, Smith and Montgomery (2016) argued that the importance of diabatic heating within the high inertial stability region is not due to the heating efficiency, but rather due to the induced secondary circulation and associated inflow at the RMW that draws angular momentum surfaces inward above the frictional boundary layer.

### c. Intensity of convection

In addition to differences in the degree of precipitation and convective symmetry, there were also differences in the intensity of convection between the two cases. Figure 8 shows the 20-dBZ echo tops and contoured frequency by altitude diagrams (CFAD) of

vertical motion from P-3 TDR analyses in Bertha and Cristobal. At 2156 UTC 3 August, during Bertha's RI, echo tops reached a maximum of 12–14-km altitude in the DSL quadrant (Fig. 8a). Although the mean vertical velocity DSL was positive throughout the troposphere, vertical velocities were confined to between  $-3$  and  $5 \text{ m s}^{-1}$  (Fig. 8b). In contrast, at 2328 UTC 25 August, near the end of Cristobal's intensification, there was a broad area of echo tops exceeding 16 km DSL (Fig. 8c). The mean vertical velocity was larger, and the vertical velocity distribution was much broader than in Bertha, with downdrafts reaching  $-10 \text{ m s}^{-1}$  and updrafts exceeding  $15 \text{ m s}^{-1}$  (Fig. 8d). Similar differences in the echo tops and vertical velocity distributions were also observed during the following P-3 flight 12 h later in each storm (not shown). These results, in addition to the stronger ice-scattering signature observed in passive microwave imagery (Fig. 5), reveal that not only was Cristobal's convection more azimuthally confined than in Bertha at this time, it was also deeper with stronger updrafts and downdrafts.

The observed differences in precipitation symmetry between Bertha and Cristobal prompt the question: What enabled Bertha's precipitation to be more symmetric (and Cristobal's precipitation to be more asymmetric), despite both storms experiencing a similar shear magnitude and having a similar tilt magnitude? This question will be further explored in the following sections.

## 5. Thermodynamic asymmetries

### a. The impact of convective downdrafts

#### 1) CRISTOBAL

Figures 9a and 9b show the lower-tropospheric equivalent potential temperature  $\theta_e$  and saturation equivalent potential temperature  $\theta_{es}$  observed by dropsondes released during missions 140825I1 (P-3) and 140825N1 (G-IV) (1840–2348 UTC 25 August). A clear azimuthal asymmetry was evident, with  $\theta_e$  in the lowest 1 km maximized in the DSR quadrant and minimized in the DSL and USL quadrants, qualitatively consistent with the observational composites of Zhang et al. (2013) and the modeling results of Riemer et al. (2010, 2013) and Smith et al. (2017). The mean DSR  $\theta_e$  in the lowest 500 m was 8–10 K higher than the mean DSL  $\theta_e$ . The conditional instability of each shear-relative quadrant can be inferred by comparing the  $\theta_e$  of a pseudoadiabatically lifted parcel with the  $\theta_{es}$  of the parcel's environment (Holton 2004). Note that in the DSR quadrant, a parcel pseudoadiabatically lifted from the lowest 500 m has a  $\theta_e$  that exceeds

$\theta_{es}$  above the level of free convection (LFC), indicative of conditional instability. In contrast, in the left-of-shear quadrants, a pseudoadiabatically lifted parcel has a  $\theta_e$  lower than that  $\theta_{es}$ , indicative of conditional stability.

The observed lower-tropospheric thermodynamic asymmetry was consistent with the influence of convective downdrafts. Figures 10a and 10b show the low-level vertical velocity derived from the P-3 TDR analysis centered at 2328 UTC 25 August. To account for potential errors in the derived velocities (Reasor et al. 2009; Lorsolo et al. 2013), only vertical velocity features with magnitudes of greater than  $1 \text{ m s}^{-1}$  will be discussed here. Updrafts ranging from 3 to  $5 \text{ m s}^{-1}$  at 0.5-km altitude and from 5 to  $8 \text{ m s}^{-1}$  at 2-km altitude were present up to 60 km south of the flight-level center. Immediately east and downstream of the updrafts was a region of  $2\text{--}4 \text{ m s}^{-1}$  downdrafts at both 0.5- and 2-km altitude. Figures 10c–f show vertical profiles of  $\theta_e$  from four dropsondes released nearly concurrently with the TDR analysis. These dropsondes were located downstream of the downdrafts (Figs. 10a,b). Each of these dropsondes showed a well-defined  $\theta_e$  minimum near or below 500-m altitude overlain by a  $\partial\theta_e/\partial z > 0$  layer, contrasting with the  $\partial\theta_e/\partial z < 0$  observed upstream in the DSR quadrant (Fig. 9b). This implies that the downdrafts injected low  $\theta_e$  air from above down into the boundary layer. Similar near-surface  $\theta_e$  minima attributed to downdrafts in tropical cyclones have also been observed in prior studies (Barnes et al. 1983; Powell 1990; Didlake and Houze 2009; Molinari et al. 2013; Dolling and Barnes 2014). Figure 11 shows two southwest–northeast vertical cross sections through the downdraft region. Negative vertical velocities of at least  $-1 \text{ m s}^{-1}$  extended up to approximately 5–7-km altitude. These downdrafts were collocated with regions of high LF radar reflectivity (not shown), indicative of heavy precipitation. Although the TDR reflectivity within and immediately upstream of the downdrafts dropped to below 30 dBZ (Fig. 11a), the corresponding LF reflectivity showed no such reflectivity decrease, implying that the relatively low TDR values near the downdrafts were due to beam attenuation.

Consistent with Zhang et al. (2013), the above results describe the following sequence of events: convective downdrafts transported low moist entropy air into the boundary layer, resulting in decreased  $\theta_e$  left of shear. As air traveled cyclonically around the TC center, surface enthalpy fluxes act to increase boundary layer  $\theta_e$  in the upshear quadrants until  $\theta_e$  reached a maximum DSR, where convection began to initiate. Thus, the convective downdrafts may have helped perpetuate the precipitation asymmetry by cooling and stabilizing

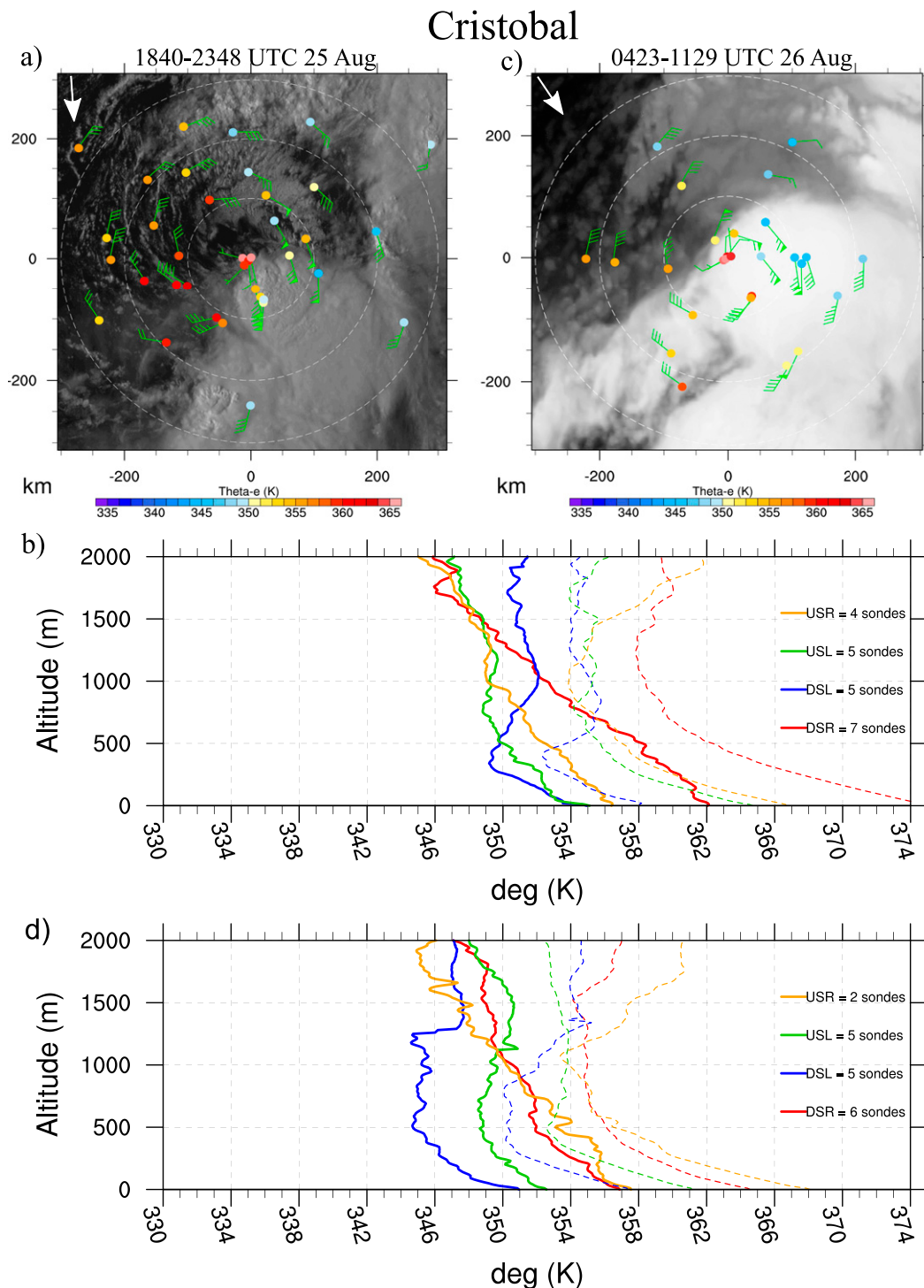


FIG. 9. (a) Equivalent potential temperature  $\theta_e$  (color, K) and TC-relative winds averaged over the lowest 500 m in Cristobal during NOAA missions 140825I1 and 140825N1 (1840–2348 UTC 25 Aug), plotted on visible satellite image at 2030 UTC 25 Aug. Range rings are every 100 km. (b) Mean  $\theta_e$  (solid) and  $\theta_{es}$  (dashed) profiles in each shear-oriented quadrant within 25–200-km radii during missions 140825I1 and 140825N1. (c) As in (a), but during NOAA mission 140826H1 and AF mission 140826U1 (0423–1129 UTC 26 Aug), plotted on infrared satellite image shown at 0930 UTC 26 Aug. (d) As in (b), but during mission 140826H1 and 140826U1. Shear vector is shown at top left of (a) and (c).



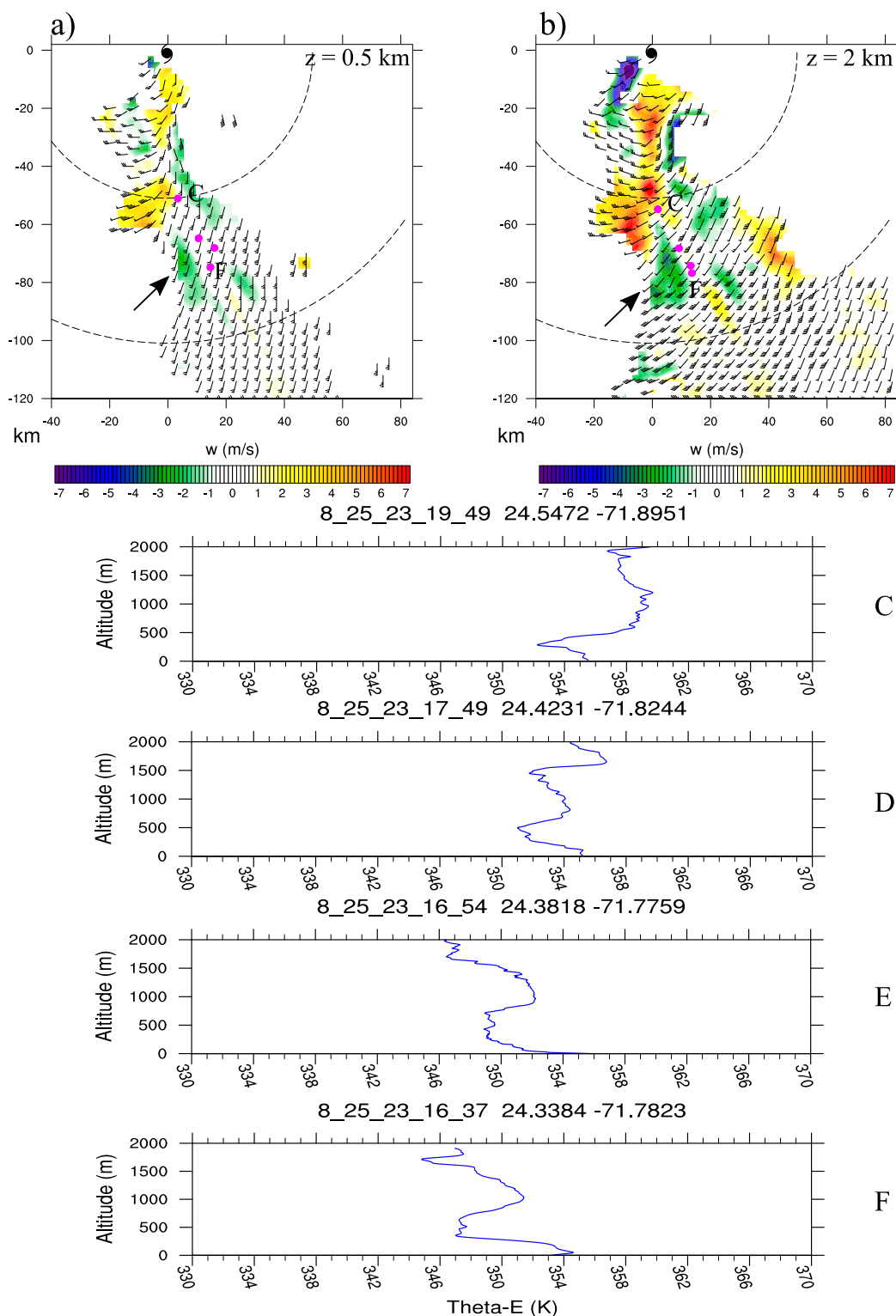


FIG. 10. Vertical motion (shaded) derived from P-3 tail Doppler radar analysis centered at 2328 UTC 25 Aug at (a) 0.5-km altitude and (b) 2-km altitude. Four dropsondes released concurrently with the TDR analysis are indicated by pink dots. (c)–(f) Vertical profiles of  $\theta_e$  from the four dropsondes.



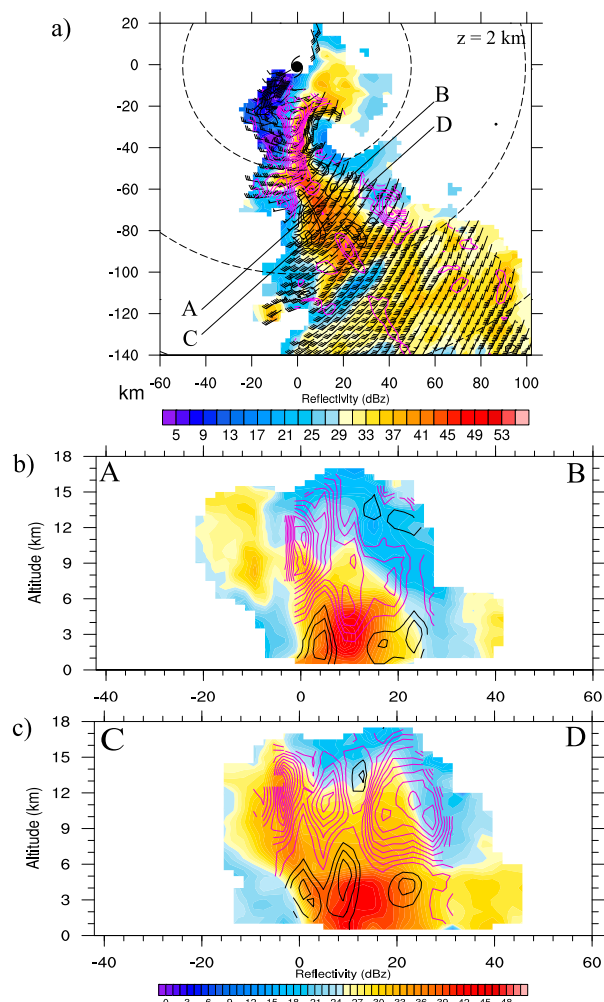


FIG. 11. (a) Reflectivity (shaded, dBZ), upward vertical velocity (magenta contours,  $1 \text{ m s}^{-1}$  interval starting at  $1 \text{ m s}^{-1}$ ), TC-relative winds, and downward vertical velocity (black contours,  $1 \text{ m s}^{-1}$  interval starting at  $-1 \text{ m s}^{-1}$ ) derived from P-3 tail Doppler radar analysis at 2328 UTC 25 Aug at 2-km altitude. (b),(c) Southwest-northeast vertical cross sections taken along the line segments indicated in (a).

the lower troposphere in the left-of-shear and upshear quadrants, preventing updrafts from achieving buoyancy and growing in those quadrants. Indeed, in the following 12 h, the precipitation and convection was not able to propagate into the upshear quadrants (Fig. 5f). In addition, not only did the asymmetric  $\theta_e$  distribution persist 12 h later, but  $\theta_e$  in the lowest 1 km also decreased in all quadrants by an average of 2–3 K (Figs. 9c,d). Sea surface temperatures beneath the storm did not appear to decrease during this period (Fig. 2). Instead, this boundary layer  $\theta_e$  decrease in all quadrants likely indicates that the downward fluxes of low  $\theta_e$  air into the boundary layer and subsequent

azimuthal advection overwhelmed the recovery of  $\theta_e$  via surface enthalpy fluxes.

## 2) BERTHA

Figures 12a and 12b show the low-tropospheric  $\theta_e$  observed by dropsondes released during missions 140803H1 (P-3), 140803N1 (G-IV), and 140803U2 (AFRC-130) (1910 UTC 3 August–0059 UTC 4 August). As in Cristobal, near-surface  $\theta_e$  was generally maximized DSR and minimized left of shear. However, the difference between the DSR and USL mean near-surface  $\theta_e$  was only about 4–6 K compared to 8–10 K in Cristobal. Also, in contrast to Cristobal (Figs. 9b,d), all shear-relative quadrants were conditionally unstable, with the pseudoadiabatically lifted parcel's  $\theta_e$  exceeding the parcel environment's  $\theta_{es}$ . The azimuthal asymmetry in near-surface  $\theta_e$  increased during mission 140804I1 12 h later, near the end of the RI period (Fig. 1b), with the mean DSR near-surface  $\theta_e$  exceeding the mean USL near-surface  $\theta_e$  by 8–9 K (Figs. 12c,d). The USL quadrant became conditionally stable, but the remaining three shear-relative quadrants remained conditionally unstable. These results were consistent with the weaker downdraft activity in Bertha, both during the 140803H1 mission (Fig. 8b) and the mission 12 h later (not shown), which resulted in less injections of low  $\theta_e$  into the boundary layer left of shear. This allowed Bertha's left-of-shear and upshear quadrants to remain convectively unstable, and may have contributed to Bertha's less asymmetric precipitation structure compared to Cristobal's.

## b. Subsidence

In addition to the cooling and stabilizing of the lower troposphere downstream of convection, subsidence may have also helped hinder the symmetrization of precipitation. Figure 13 shows the mean and individual skew  $T$ -log $p$  profiles in each shear-oriented quadrant within 25–200-km radii during the 140825I1 and 140825N1 missions into Cristobal. Following Zawislak et al. (2016), layers with a sharp increase with height in both potential temperature and dewpoint depression indicate adiabatic warming and drying as a result of subsidence. The mean USR and DSR profiles depict a layer between 850 and 750 hPa (1.5–2.5-km altitude) that features a more rapid upward increase in potential temperature and a larger dewpoint depression than the adjacent layers above and below. This signature was more pronounced in the individual profiles between 1.5- and 3-km altitude. The observed isothermal or inversion layer helps to act as a lid, capping the boundary layer and preventing shallow updrafts from growing in the USR and DSR quadrants, thus

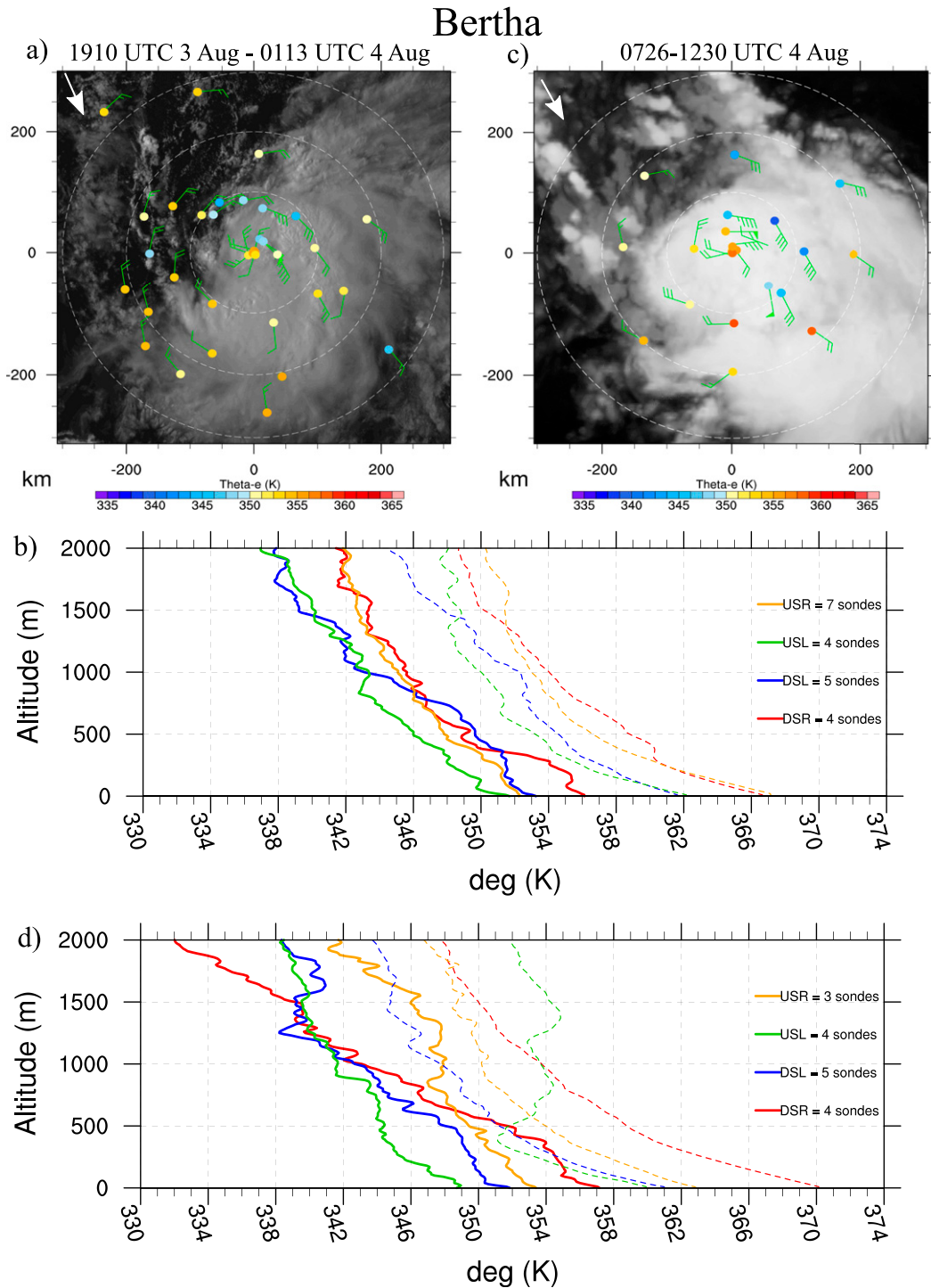


FIG. 12. As in Fig. 9, but in Bertha during (a),(b) NOAA missions 140803H1, 140803N1, and AF mission 140803U2 (1910 UTC 3 Aug–0113 UTC 4 Aug) plotted on visible satellite image at 2045 UTC 3 Aug; and (c),(d) mission 140804I1 (0726–1230 UTC 4 Aug) plotted on infrared satellite image at 1030 UTC 4 Aug.

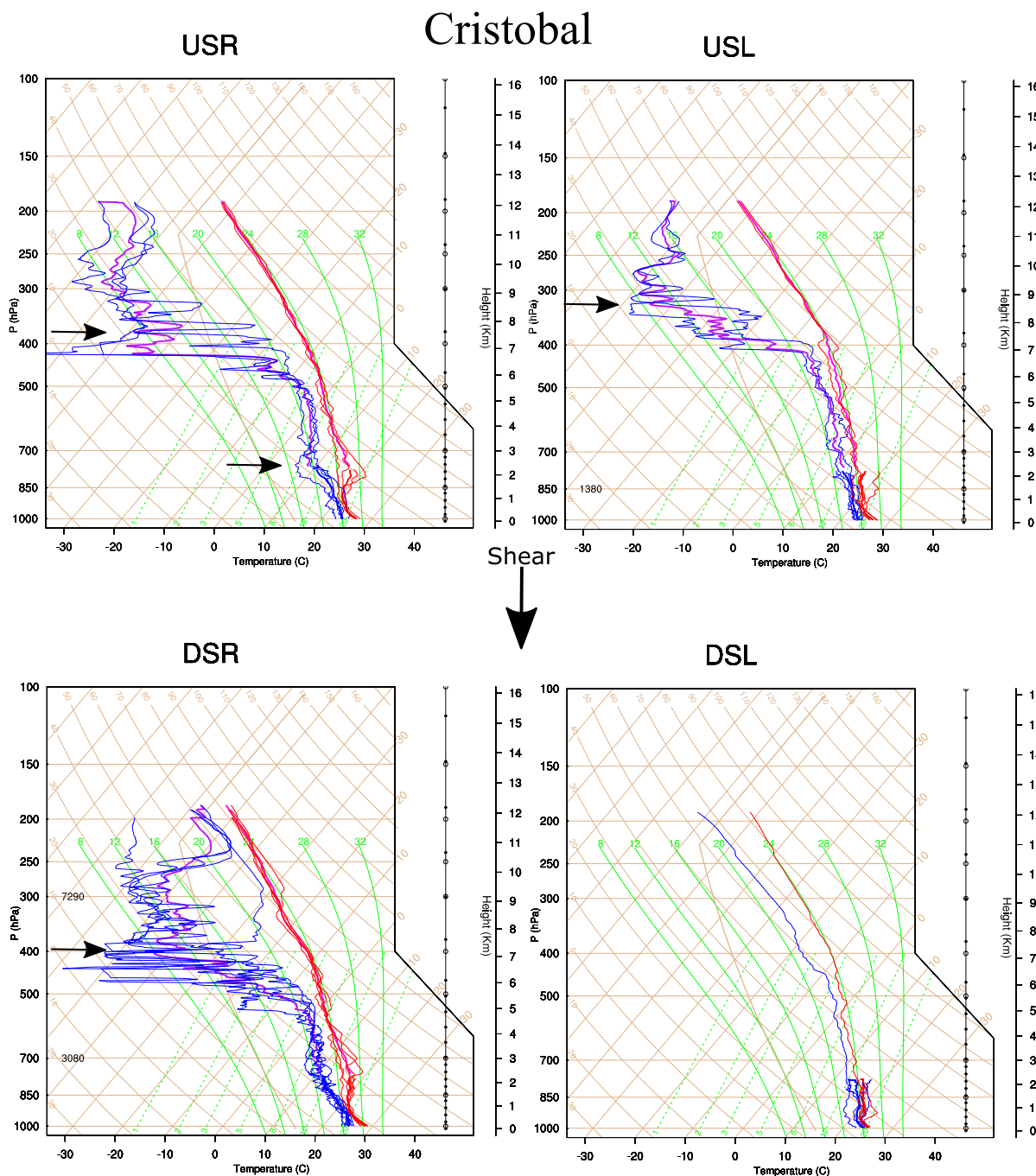


FIG. 13. Mean (thick lines) and individual (thin lines) skew  $T$ -log $p$  profiles in each shear-oriented quadrant within 25–200-km radii during missions 140825I1 and 140825N1 (1840–2348 UTC 25 Aug) in Cristobal. Shear vector points downward.

preventing the precipitation in Cristobal from becoming more symmetrically distributed. Dropsonde profiles within Bertha during the 140803H1 and 140803N1 missions did not appear to exhibit subsidence (Fig. 14), consistent with its more symmetrically distributed precipitation at that time (Figs. 6a,b).

This subsidence could be the result of a couple different mechanisms. One possibility is that as the potential vorticity column associated with the TC vortex is tilted by the environmental shear, a cool (warm) anomaly develops downtilt (uptilt) via adiabatic ascent (descent) as required to keep the tilted vortex balanced

## Bertha

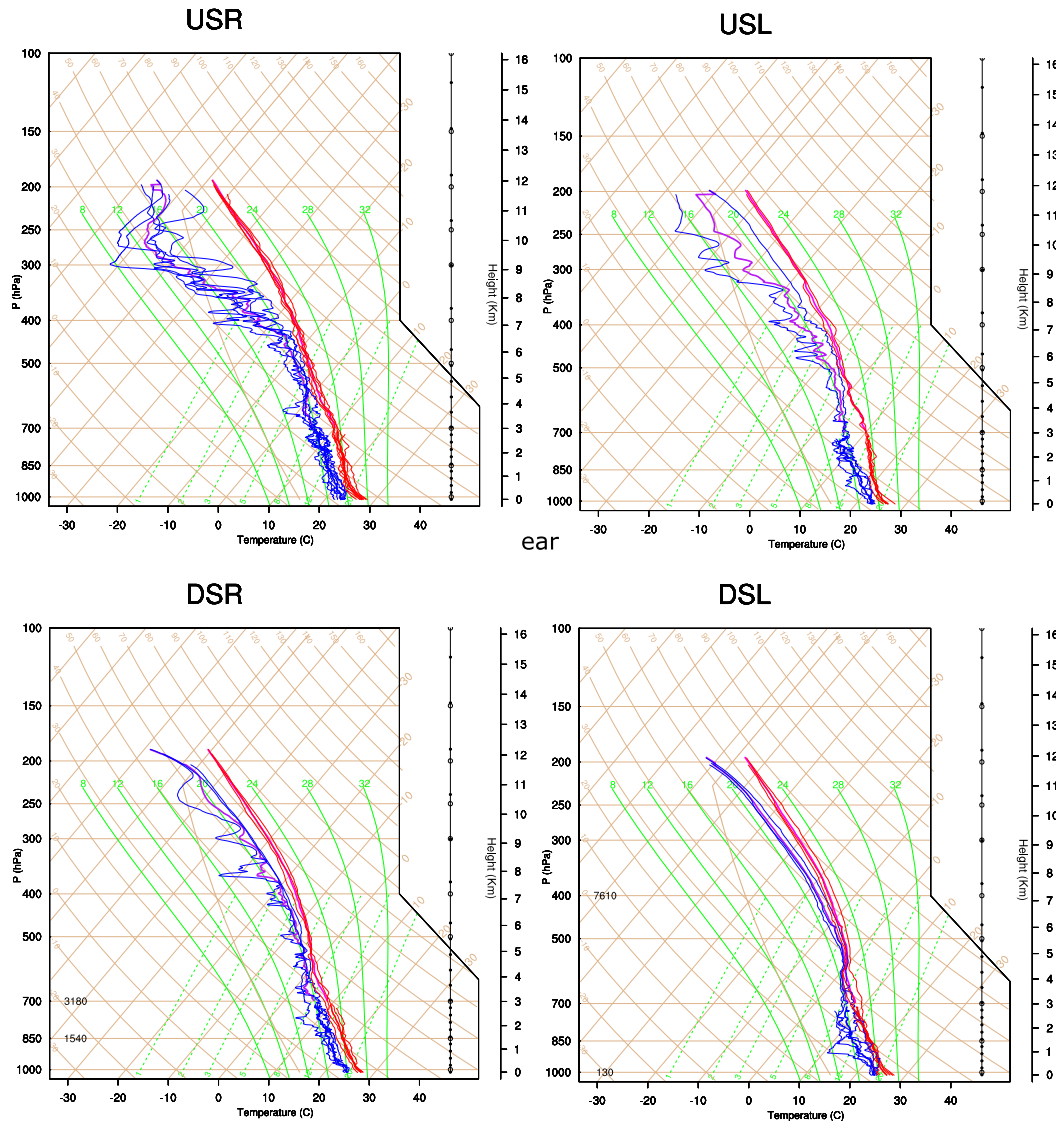


FIG. 14. As in Fig. 13, but during missions 140803H1 and 140803N1 (1910 UTC 3 Aug–0059 UTC 4 Aug) in Bertha.

(Jones 1995; DeMaria 1996). The vortex's cyclonic flow then interacts with these temperature anomalies, resulting in isentropic ascent to the right of downtilt and isentropic descent to the left of downtilt. Another possibility is that the subsidence was the result of light stratiform precipitation falling and evaporating beneath the anvil region, as observed by Dolling and Barnes (2012) and Kerns and Chen (2015). Inspection of the LF and TDR reflectivity (Fig. 6a), as well as visible satellite imagery (Fig. 9a), showed that the upshear quadrants of Cristobal were nearly precipitation-free and nearly devoid of clouds. This would suggest that the subsidence was more likely associated with the

descending branch of the asymmetric secondary circulation in response to the vortex tilt.

### c. Azimuthal distribution of midtropospheric relative humidity

Bertha and Cristobal exhibited substantial differences in the azimuthal distribution of midtropospheric relative humidity. Figure 15 shows GOES-13 6.7- $\mu\text{m}$  channel (water vapor) satellite images of Bertha and Cristobal, with 8-km TC-relative winds overlaid. Cristobal was embedded within a much drier environment in the mid- to upper troposphere, particularly in the upshear quadrants. Dropsonde skew  $T$ -log $p$



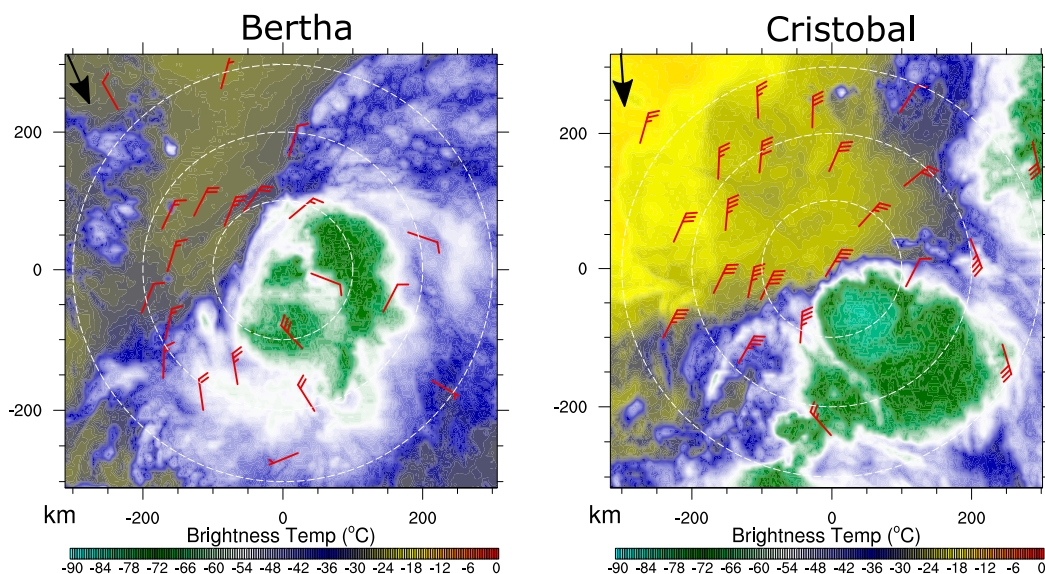


FIG. 15. *GOES-13* 6.7- $\mu\text{m}$  channel (water vapor) satellite image with 8-km TC-relative winds from dropsondes of (a) Bertha at 2045 UTC 3 Aug and (b) Cristobal at 2030 UTC 25 Aug. Shear vector is shown at top left. Range rings are every 100 km.

(Figs. 13–14) and vertical RH profiles (not shown) showed that the USL through DSR quadrants in Cristobal were much drier than in Bertha in two distinct layers, most prominently above 6-km altitude and more subtly at 2–3-km altitude. The extremely dry air above 6-km altitude appeared to be laterally advected in from the environment by 10–15  $\text{m s}^{-1}$  TC-relative inflow upshear (Fig. 15b). Both dropsonde observations from the G-IV flight and water vapor satellite imagery 24 h earlier did not show this mid- to upper-tropospheric dry air within 300 km of the TC center, further supporting this interpretation. This is consistent with the midlevel ventilation mechanism described by Tang and Emanuel (2010). This upshear inflow was likely due to the north-northeasterly TC-relative environmental flow (Fig. 4d) associated with a midlatitude trough to the north (Fig. 3c). This was also consistent with the larger shear within the 4–7-km layer in Cristobal (Fig. 4e). In contrast, the TC-relative flow at 2.5-km altitude in Cristobal was quite weak (not shown), indicating that the drier air at 2–3-km altitude was not due to lateral advection. More likely, this drying was due to the subsidence discussed in section 5b.

## 6. Summary and discussion

### a. Summary of two cases

Airborne observations from NOAA and Air Force Reserve aircraft were used to document the structural evolutions of two tropical cyclones at strong tropical

storm intensity, Bertha and Cristobal (2014), which experienced 9–12  $\text{m s}^{-1}$  of northerly to northwesterly environmental vertical wind shear. Both storms showed an azimuthal asymmetry in precipitation, consistent with prior studies (e.g., Reasor et al. 2013; Rogers et al. 2013). Bertha in particular had precipitation occur within the high inertial stability region inside the radius of maximum wind. Such a configuration has been demonstrated to be associated with intensification by many theoretical (e.g., Schubert and Hack 1982; Pendergrass and Willoughby 2009; Vigh and Schubert 2009) and observational studies (e.g., Nguyen and Molinari 2012; Rogers et al. 2013; Stevenson et al. 2014; Rogers et al. 2015). Notably, Bertha's precipitation was more symmetrically distributed and extended into the upshear quadrants, while Cristobal's was strictly confined to the DSL quadrant.

Although both Bertha and Cristobal were unable to intensify into a major hurricane ( $>50 \text{ m s}^{-1}$ ), an important question to address is why some sheared TCs develop a more symmetric precipitation distribution (i.e., Bertha) while other sheared TCs do not (i.e., Cristobal). Observational studies have found that tropical cyclones with a more symmetric precipitation distribution are generally more likely to intensify (Kieper and Jiang 2012; Rogers et al. 2013; Zagrodnik and Jiang 2014; Tao and Jiang 2015; Alvey et al. 2015). This is consistent with theoretical studies showing that TC intensity change is most sensitive to the axisymmetric



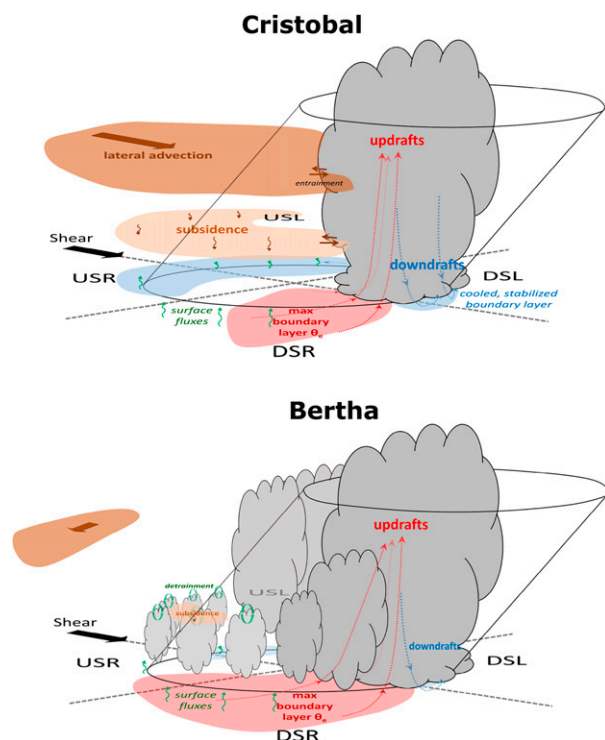


FIG. 16. Three-dimensional schematics summarizing the hypothesized hindrances to precipitation symmetry in tropical cyclones. The top schematic depicts the more asymmetric case (Cristobal), while the bottom schematic depicts the more symmetric case (Bertha).

(azimuthal wavenumber 0) component of diabatic heating (e.g., Nolan and Grasso 2003; Nolan et al. 2007).

#### b. Hypothesized hindrances to precipitation symmetry

Figure 16 summarizes the potential hindrances to precipitation symmetry based on observations collected in Bertha and Cristobal while at tropical storm intensity: (i) convective downdrafts that cool and stabilize the lower troposphere downstream in the left-of-shear and upshear quadrants; (ii) subsidence in the upshear quadrants, which acts not only to cap the boundary layer, but also reduces the midtropospheric relative humidity; and (iii) lateral advection of dry air from the environment into the TC's upshear quadrants.

##### 1) CONVECTIVE DOWNDRAFTS

Observations near the end of Cristobal's intensification showed that downdrafts in Cristobal's DSL quadrant were more prevalent and more intense than in Bertha's. This enhanced downdraft activity was associated with more intense DSL convection in Cristobal, evidenced by stronger updrafts and higher echo tops (exceeding 18-km altitude). These downdrafts

deposited low  $\theta_e$  air into the boundary layer, cooling and stabilizing the lower troposphere in the left-of-shear and upshear regions. As boundary layer air traveled cyclonically around the storm, new convection was unable to initiate until air reached the downshear region. This was where the accumulated warming/moistening effects of surface enthalpy fluxes and resulting destabilization were finally sufficient for convective initiation to occur. Because convective initiation was impeded over a large azimuthal swath, Cristobal was unable to achieve a more symmetric convective structure that typically favors further TC intensification. Recent idealized three-dimensional (Riemer et al. 2010, 2013) and axisymmetric (Tang and Emanuel 2012) simulations demonstrated the role of convective downdrafts outside the eyewall in the weakening of sheared, mature TCs. In those simulations, downdrafts transported low entropy air into the inflow layer, and this low entropy air was swept inward into the eyewall region, resulting in a reduction of mean eyewall  $\theta_e$ . Here, it is shown that convective downdrafts within the inner-core region near the RMW, as opposed to well outside the RMW, can detrimentally affect developing TCs by impeding the development of a more symmetric diabatic heating distribution. This is consistent with Barnes et al.'s (1983) speculation that downdraft cooling played a role in Hurricane Floyd's (1981) asymmetric reflectivity distribution.

The downdrafts at the end of Cristobal's intensification period occurred during a period of more intense convection. This suggests that intense convection may not necessarily lead to the intensification of sheared tropical cyclones if the negative effects of stronger lower-tropospheric downdrafts can offset or override the positive effects of upper-level warming (e.g., Guimond et al. 2010; Chen and Zhang 2013) and vortex stretching (e.g., Hendricks et al. 2004; Montgomery et al. 2006). Within sheared TCs, the convective downdrafts can be invigorated by and/or transport downward the midtropospheric low  $\theta_e$  air that has penetrated into the inner core through either midlevel ventilation (Simpson and Riehl 1958; Tang and Emanuel 2010; Dolling and Barnes 2014) or subsidence resulting from the interaction of the cyclonic flow with the uptilt warm anomaly (Jones 1995). The notion that intense convection within sheared TCs may in some cases be detrimental to subsequent TC intensification due to enhanced downdrafts is consistent with DeMaria et al. (2012), which found that the largest inner-core lightning densities occurred in sheared TCs that struggled to intensify.

Surface enthalpy fluxes can help counteract the negative effects of downdrafts. Studies of Hurricane Edouard (2014) have highlighted the importance of warm sea surface temperatures to the boundary layer recovery downwind of convection during the intensification and subsequent weakening periods (Rogers et al. 2016; Zawislak et al. 2016; Zhang et al. 2017). Recent idealized studies have also emphasized the importance of enhanced surface winds and latent heat fluxes left of shear in helping sheared TCs achieve a more symmetric precipitation distribution (Rappin and Nolan 2012; Onderlinde and Nolan 2016). This implies a complex interplay between asymmetric convection, convective downdrafts, and surface enthalpy fluxes in determining the net contribution of the boundary layer thermodynamic condition to precipitation symmetry and TC intensity change.

## 2) SUBSIDENCE AND LATERAL ADVECTION OF ENVIRONMENTAL DRY AIR IN THE UPSHEAR QUADRANTS

Dropsonde observations implied the presence of subsidence in the upshear and right-of-shear quadrants near the end of Cristobal's intensification. Subsidence warming can result in the formation of an isothermal or inversion layer that caps the boundary layer, which helps prevent shallow updrafts from growing. Subsidence can also result in the reduction of low- to midtropospheric relative humidity. The subsidence in the upshear quadrants could be due to isentropic descent as cyclonic flow interacts with the uptilt warm anomaly (Jones 1995), light stratiform precipitation evaporating in unsaturated air under the anvil region (Dolling and Barnes 2012; Kerns and Chen 2015), or both. In Cristobal's case, the subsidence did not appear to occur in precipitating areas, so it was more likely due to isentropic descent. The spatial and temporal coverage of the observations were too limited to conduct a quantitative analysis of these potential contributing factors. Regardless of the cause, subsidence in the upshear quadrants can be another contributing factor to the lack of precipitation symmetry.

The USL through DSR quadrants in Cristobal were also much drier above 6-km altitude than in Bertha. This drier air appeared to be the result of midlevel ventilation (Tang and Emanuel 2010), consistent with the larger environmental vertical wind shear within the 4–7-km layer. The upshear inflow responsible for importing this dry air was likely a combination of the TC-relative environmental flow associated with a midlatitude trough to the north and the flow associated with the tilted TC vortex.

Whether arising from vortex-scale subsidence or from midlevel ventilation, midtropospheric dry air upshear can be detrimental to precipitation symmetry in a couple possible ways. First, the midlevel dry air is entrained into the precipitating region, so it could invigorate evaporation-driven downdrafts that transport low entropy air into the boundary layer (e.g., Gilmore and Wicker 1998; Molinari et al. 2013). Assuming no entrainment, the vertical  $\theta_e$  profiles in Cristobal (Fig. 9b) imply that the downdraft-cooled air originated from at least 1.5-km altitude, as the mean DSL  $\theta_e$  at 300-m altitude was equivalent to the mean DSR  $\theta_e$  at 1.5-km altitude. At least some entrainment occurred in reality, however, so the near-surface low- $\theta_e$  air may have originated from well above 1.5-km altitude. As a result, the relative importance of the dry air at 2–3-km altitude versus above 6-km altitude in invigorating the downdrafts is unclear. On the other hand, recent idealized simulations (James and Markowski 2010; Kilroy and Smith 2013) have shown that dry air above the boundary layer does not increase downdraft and cold pool strength. Instead, dry air enhances entrainment, reducing the updraft strength and hydrometeor mass. The effects of reduced hydrometeor mass on reducing diabatic cooling overwhelms the effects of the dry air on enhancing diabatic cooling, resulting in reduced negative buoyancy and weaker downdrafts. The lack of reflectivity in the upshear quadrants in both the LF radar and TDR, and the presence of only shallow cumuli upshear in visible satellite imagery (Fig. 9a) suggest that in this particular case, the dry, statically stable layer at the more shallow 2–3-km altitude was more likely to play a role in stunting updraft growth. Regardless of the exact mechanisms, midtropospheric dry air upshear clearly is a detriment to precipitation and diabatic heating symmetry, as shown here and in other recent studies (Zawislak et al. 2016; Rogers et al. 2016; Rios-Berrios and Torn 2017).

Bertha did become markedly more asymmetric on passive microwave imagery and P-3 LF reflectivity after 1200 UTC 4 August, corresponding with the end of its rapid intensification. This occurred prior to the increase in shear (Fig. 1b) and decrease in SST (Fig. 2b). Unfortunately, the G-IV aircraft was not flying during that time period, so there were insufficient dropsonde observations through the depth of the troposphere to assess to what extent the above proposed mechanisms impacted the increase in precipitation asymmetry observed after Bertha's peak in intensity.

## c. Future work

Several potential mechanisms that can inhibit precipitation symmetry have been presented, but the relative importance of these mechanisms in inhibiting the

development of precipitation symmetry remains unresolved, although it should be noted that these hypothesized mechanisms are not mutually exclusive and can interact with one another. Tail Doppler radar and dropsonde observations could be used to assess these mechanisms in additional cases and within a composite framework, but the spatial and temporal discontinuities of these observations make it difficult to assess possible interactions between these mechanisms. Analysis of high-resolution numerical model simulations could be one way to fill in these gaps. Finally, vortex tilt could also play a role: as the vortex becomes more tilted, it becomes increasingly difficult for evaporating hydrometeors to be advected into and moisten the upshear quadrants (Rappin and Nolan 2012).

**Acknowledgments.** The authors thank Jonathan Zawislak, Jun Zhang, Gary Barnes, and two anonymous reviewers for their helpful comments on this manuscript. The first author was supported by a National Research Council research associateship award.

## REFERENCES

- Alvey, G. R., III, J. Zawislak, and E. Zipser, 2015: Precipitation properties observed during tropical cyclone intensity change. *Mon. Wea. Rev.*, **143**, 4476–4492, doi:[10.1175/MWR-D-15-0065.1](https://doi.org/10.1175/MWR-D-15-0065.1).
- Barnes, G. M., E. J. Zipser, D. Jorgensen, and F. Marks Jr., 1983: Mesoscale and convective structure of a hurricane rainband. *J. Atmos. Sci.*, **40**, 2125–2137, doi:[10.1175/1520-0469\(1983\)040<2125:MACSOA>2.0.CO;2](https://doi.org/10.1175/1520-0469(1983)040<2125:MACSOA>2.0.CO;2).
- Bender, M., 1997: The effect of relative flow on the asymmetric structure in the interior of hurricanes. *J. Atmos. Sci.*, **54**, 703–724, doi:[10.1175/1520-0469\(1997\)054<0703:TEORFO>2.0.CO;2](https://doi.org/10.1175/1520-0469(1997)054<0703:TEORFO>2.0.CO;2).
- Blake, E., 2015: Tropical cyclone report: Hurricane Bertha (1–6 August 2014). Rep. AL032014, National Hurricane Center, 16 pp., [http://www.nhc.noaa.gov/data/tcr/AL032014\\_Bertha.pdf](http://www.nhc.noaa.gov/data/tcr/AL032014_Bertha.pdf).
- Bogner, P. B., G. M. Barnes, and J. L. Franklin, 2000: Conditional instability and shear for six hurricanes over the Atlantic Ocean. *Wea. Forecasting*, **15**, 192–207, doi:[10.1175/1520-0434\(2000\)015<0192:CIASFS>2.0.CO;2](https://doi.org/10.1175/1520-0434(2000)015<0192:CIASFS>2.0.CO;2).
- Braun, S. A., M. T. Montgomery, and Z. Pu, 2006: High-resolution simulation of Hurricane Bonnie (1998). Part I: The organization of eyewall vertical motion. *J. Atmos. Sci.*, **63**, 19–42, doi:[10.1175/JAS3598.1](https://doi.org/10.1175/JAS3598.1).
- Chen, H., and D. L. Zhang, 2013: On the rapid intensification of Hurricane Wilma (2005). Part II: Convective bursts and the upper-level warm core. *J. Atmos. Sci.*, **70**, 146–162, doi:[10.1175/JAS-D-12-062.1](https://doi.org/10.1175/JAS-D-12-062.1).
- Chen, S. S., J. A. Knaff, and F. D. Marks, 2006: Effects of vertical wind shear and storm motion on tropical cyclone rainfall asymmetries deduced from TRMM. *Mon. Wea. Rev.*, **134**, 3190–3208, doi:[10.1175/MWR3245.1](https://doi.org/10.1175/MWR3245.1).
- Corbosiero, K. L., and J. Molinari, 2002: The effects of vertical wind shear on the distribution of convection in tropical cyclones. *Mon. Wea. Rev.*, **130**, 2110–2123, doi:[10.1175/1520-0493\(2002\)130<2110:TEOVWS>2.0.CO;2](https://doi.org/10.1175/1520-0493(2002)130<2110:TEOVWS>2.0.CO;2).
- Davis, C. A., S. C. Jones, and M. Riemer, 2008: Hurricane vortex dynamics during Atlantic extratropical transition. *J. Atmos. Sci.*, **65**, 714–736, doi:[10.1175/2007JAS2488.1](https://doi.org/10.1175/2007JAS2488.1).
- DeHart, J. C., R. A. Houze, and R. F. Rogers, 2014: Quadrant distribution of tropical cyclone inner-core kinematics in relation to environmental shear. *J. Atmos. Sci.*, **71**, 2713–2732, doi:[10.1175/JAS-D-13-0298.1](https://doi.org/10.1175/JAS-D-13-0298.1).
- DeMaria, M., 1996: The effect of vertical shear on tropical cyclone intensity change. *J. Atmos. Sci.*, **53**, 2076–2088, doi:[10.1175/1520-0469\(1996\)053<2076:TEOVSO>2.0.CO;2](https://doi.org/10.1175/1520-0469(1996)053<2076:TEOVSO>2.0.CO;2).
- , and J. Kaplan, 1994: A Statistical Hurricane Intensity Prediction Scheme (SHIPS) for the Atlantic basin. *Wea. Forecasting*, **9**, 209–220, doi:[10.1175/1520-0434\(1994\)009<0209:ASHIPS>2.0.CO;2](https://doi.org/10.1175/1520-0434(1994)009<0209:ASHIPS>2.0.CO;2).
- , R. T. DeMaria, J. A. Knaff, and D. Molenaar, 2012: Tropical cyclone lightning and rapid intensity change. *Mon. Wea. Rev.*, **140**, 1828–1842, doi:[10.1175/MWR-D-11-00236.1](https://doi.org/10.1175/MWR-D-11-00236.1).
- , C. R. Sampson, J. A. Knaff, and K. D. Musgrave, 2014: Is tropical cyclone intensity guidance improving? *Bull. Amer. Meteor. Soc.*, **95**, 387–398, doi:[10.1175/BAMS-D-12-00240.1](https://doi.org/10.1175/BAMS-D-12-00240.1).
- Didlake, A. C., Jr., and R. A. Houze Jr., 2009: Convective-scale downdrafts in the principal rainband of Hurricane Katrina (2005). *Mon. Wea. Rev.*, **137**, 3269–3293, doi:[10.1175/2009MWR2827.1](https://doi.org/10.1175/2009MWR2827.1).
- Dolling, K., and G. M. Barnes, 2012: Warm-core formation in Tropical Storm Humberto (2001). *Mon. Wea. Rev.*, **140**, 1177–1190, doi:[10.1175/MWR-D-11-00183.1](https://doi.org/10.1175/MWR-D-11-00183.1).
- , and —, 2014: The evolution of Hurricane Humberto (2001). *J. Atmos. Sci.*, **71**, 1276–1291, doi:[10.1175/JAS-D-13-0164.1](https://doi.org/10.1175/JAS-D-13-0164.1).
- Finocchio, P. M., and S. J. Majumdar, 2017: A statistical perspective on wind profiles and vertical wind shear in tropical cyclone environments of the Northern Hemisphere. *Mon. Wea. Rev.*, **145**, 361–378, doi:[10.1175/MWR-D-16-0221.1](https://doi.org/10.1175/MWR-D-16-0221.1).
- , —, D. S. Nolan, and M. Iskandarani, 2016: Idealized tropical cyclone responses to the height and depth of environmental vertical wind shear. *Mon. Wea. Rev.*, **144**, 2155–2175, doi:[10.1175/MWR-D-15-0320.1](https://doi.org/10.1175/MWR-D-15-0320.1).
- Frank, W. M., and E. A. Ritchie, 2001: Effects of vertical wind shear on the intensity and structure of numerically simulated hurricanes. *Mon. Wea. Rev.*, **129**, 2249–2269, doi:[10.1175/1520-0493\(2001\)129<2249:EOVWSO>2.0.CO;2](https://doi.org/10.1175/1520-0493(2001)129<2249:EOVWSO>2.0.CO;2).
- Galareau, T. J., and C. A. Davis, 2013: Diagnosing forecast errors in tropical cyclone motion. *Mon. Wea. Rev.*, **141**, 405–430, doi:[10.1175/MWR-D-12-00071.1](https://doi.org/10.1175/MWR-D-12-00071.1).
- Gamache, J. F., 1997: Evaluation of a fully three-dimensional variational Doppler analysis technique. Preprints, *28th Conf. on Radar Meteorology*, Austin, TX, Amer. Meteor. Soc., 422–423.
- Ge, X., T. Li, and M. Peng, 2013: Effects of vertical shears and midlevel dry air on tropical cyclone developments. *J. Atmos. Sci.*, **70**, 3859–3875, doi:[10.1175/JAS-D-13-066.1](https://doi.org/10.1175/JAS-D-13-066.1).
- Gilmore, M. S., and L. J. Wicker, 1998: The influence of midtropospheric dryness on supercell morphology and evolution. *Mon. Wea. Rev.*, **126**, 943–958, doi:[10.1175/1520-0493\(1998\)126<0943:TIOMDO>2.0.CO;2](https://doi.org/10.1175/1520-0493(1998)126<0943:TIOMDO>2.0.CO;2).
- Guimond, S. R., G. M. Heymsfield, and F. J. Turk, 2010: Multiscale observations of Hurricane Dennis (2005): The effects of hot towers on rapid intensification. *J. Atmos. Sci.*, **67**, 633–654, doi:[10.1175/2009JAS3119.1](https://doi.org/10.1175/2009JAS3119.1).
- Hendricks, E. A., M. T. Montgomery, and C. A. Davis, 2004: The role of “vortical” hot towers in the formation of Tropical Cyclone Diana (1984). *J. Atmos. Sci.*, **61**, 1209–1232, doi:[10.1175/1520-0469\(2004\)061<1209:TROVHT>2.0.CO;2](https://doi.org/10.1175/1520-0469(2004)061<1209:TROVHT>2.0.CO;2).

- Hock, T. F., and J. L. Franklin, 1999: The NCAR GPS dropwindsonde. *Bull. Amer. Meteor. Soc.*, **80**, 407–420, doi:[10.1175/1520-0477\(1999\)080<0407:TNGD>2.0.CO;2](https://doi.org/10.1175/1520-0477(1999)080<0407:TNGD>2.0.CO;2).
- Holton, J. R., 2004: *An Introduction to Dynamic Meteorology*. 4th ed. International Geophysical Series, Vol. 88, Elsevier Academic Press, 535 pp.
- James, R. P., and P. M. Markowski, 2010: A numerical investigation of the effects of dry air aloft on deep convection. *Mon. Wea. Rev.*, **138**, 140–161, doi:[10.1175/2009MWR3018.1](https://doi.org/10.1175/2009MWR3018.1).
- Jones, S. C., 1995: The evolution of vortices in vertical shear. I: Initially barotropic vortices. *Quart. J. Roy. Meteor. Soc.*, **121**, 821–851, doi:[10.1002/qj.49712152406](https://doi.org/10.1002/qj.49712152406).
- Kaplan, J., and M. DeMaria, 2003: Large-scale characteristics of rapidly intensifying tropical cyclones in the North Atlantic basin. *Wea. Forecasting*, **18**, 1093–1108, doi:[10.1175/1520-0434\(2003\)018<1093:LCORIT>2.0.CO;2](https://doi.org/10.1175/1520-0434(2003)018<1093:LCORIT>2.0.CO;2).
- , —, and J. A. Knaff, 2010: A revised tropical cyclone rapid intensification index for the Atlantic and eastern North Pacific basins. *Wea. Forecasting*, **25**, 220–241, doi:[10.1175/2009WAF2222280.1](https://doi.org/10.1175/2009WAF2222280.1).
- Kerns, B. W., and S. S. Chen, 2015: Subsidence warming as an underappreciated ingredient in tropical cyclogenesis. Part I: Aircraft observations. *J. Atmos. Sci.*, **72**, 4237–4260, doi:[10.1175/JAS-D-14-0366.1](https://doi.org/10.1175/JAS-D-14-0366.1).
- Kieper, M. E., and H. Jiang, 2012: Predicting tropical cyclone rapid intensification using the 37 GHz ring pattern identified from passive microwave measurements. *Geophys. Res. Lett.*, **39**, L13804, doi:[10.1029/2012GL052115](https://doi.org/10.1029/2012GL052115).
- Kilroy, G., and R. K. Smith, 2013: A numerical study of rotating convection during tropical cyclogenesis. *Quart. J. Roy. Meteor. Soc.*, **139**, 1255–1269, doi:[10.1002/qj.2022](https://doi.org/10.1002/qj.2022).
- Lorsolo, S., J. Gamache, and A. Aksoy, 2013: Evaluation of the Hurricane Research Division Doppler radar analysis software using synthetic data. *J. Atmos. Oceanic Technol.*, **30**, 1055–1071, doi:[10.1175/JTECH-D-12-00161.1](https://doi.org/10.1175/JTECH-D-12-00161.1).
- Marks, F. D., Jr., R. A. Houze Jr., and J. F. Gamache, 1992: Dual-aircraft investigation of the inner core of Hurricane Norbert. Part I: Kinematic structure. *J. Atmos. Sci.*, **49**, 919–942, doi:[10.1175/1520-0469\(1992\)049<0919:DAIOTI>2.0.CO;2](https://doi.org/10.1175/1520-0469(1992)049<0919:DAIOTI>2.0.CO;2).
- Molinari, J., and D. Vollaro, 2010: Rapid intensification of a sheared tropical storm. *Mon. Wea. Rev.*, **138**, 3869–3885, doi:[10.1175/2010MWR3378.1](https://doi.org/10.1175/2010MWR3378.1).
- , —, and K. L. Corbosiero, 2004: Tropical cyclone formation in a sheared environment: A case study. *J. Atmos. Sci.*, **61**, 2493–2509, doi:[10.1175/JAS3291.1](https://doi.org/10.1175/JAS3291.1).
- , J. Frank, and D. Vollaro, 2013: Convective bursts, downdraft cooling, and boundary layer recovery in a sheared tropical storm. *Mon. Wea. Rev.*, **141**, 1048–1060, doi:[10.1175/MWR-D-12-00135.1](https://doi.org/10.1175/MWR-D-12-00135.1).
- Montgomery, M. T., M. Nicholls, T. Cram, and A. Saunders, 2006: A “vortical” hot tower route to tropical cyclogenesis. *J. Atmos. Sci.*, **63**, 355–386, doi:[10.1175/JAS3604.1](https://doi.org/10.1175/JAS3604.1).
- Nguyen, L. T., and J. Molinari, 2012: Rapid intensification of a sheared, fast-moving hurricane over the Gulf Stream. *Mon. Wea. Rev.*, **140**, 3361–3378, doi:[10.1175/MWR-D-11-00293.1](https://doi.org/10.1175/MWR-D-11-00293.1).
- , and —, 2015: Simulation of the downshear reformation of a tropical cyclone. *J. Atmos. Sci.*, **72**, 4529–4551, doi:[10.1175/JAS-D-15-0036.1](https://doi.org/10.1175/JAS-D-15-0036.1).
- Nolan, D. S., and L. D. Grasso, 2003: Nonhydrostatic, three-dimensional perturbations to balanced, hurricane-like vortices. Part II: Symmetric response and nonlinear simulations. *J. Atmos. Sci.*, **60**, 2717–2745, doi:[10.1175/1520-0469\(2003\)060<2717:NTPTBH>2.0.CO;2](https://doi.org/10.1175/1520-0469(2003)060<2717:NTPTBH>2.0.CO;2).
- , Y. Moon, and D. P. Stern, 2007: Tropical cyclone intensification from asymmetric convection: Energetics and efficiency. *J. Atmos. Sci.*, **64**, 3377–3405, doi:[10.1175/JAS3988.1](https://doi.org/10.1175/JAS3988.1).
- Onderlinde, M. J., and D. S. Nolan, 2016: Tropical cyclone–relative helicity and the pathways to intensification in shear. *J. Atmos. Sci.*, **73**, 869–890, doi:[10.1175/JAS-D-15-0261.1](https://doi.org/10.1175/JAS-D-15-0261.1).
- Pasch, R. J., 2015: Tropical cyclone report: Hurricane Cristobal (23–29 August 2014). Rep. AL042014, National Hurricane Center, 14 pp., [http://www.nhc.noaa.gov/data/tcr/AL042014\\_Cristobal.pdf](http://www.nhc.noaa.gov/data/tcr/AL042014_Cristobal.pdf).
- Pendergrass, A. G., and H. E. Willoughby, 2009: Diabatically induced secondary flows in tropical cyclones. Part I: Quasi-steady forcing. *Mon. Wea. Rev.*, **137**, 805–821, doi:[10.1175/2008MWR2657.1](https://doi.org/10.1175/2008MWR2657.1).
- Powell, M. D., 1990: Boundary layer structure and dynamics in outer hurricane rainbands. Part II: Downdraft modification and mixed layer recovery. *Mon. Wea. Rev.*, **118**, 918–938, doi:[10.1175/1520-0493\(1990\)118<0918:BLSADI>2.0.CO;2](https://doi.org/10.1175/1520-0493(1990)118<0918:BLSADI>2.0.CO;2).
- Rappin, E. D., and D. S. Nolan, 2012: The effect of vertical shear orientation on tropical cyclogenesis. *Quart. J. Roy. Meteor. Soc.*, **138**, 1035–1054, doi:[10.1002/qj.977](https://doi.org/10.1002/qj.977).
- Reasor, P. D., and M. T. Montgomery, 2001: Three-dimensional alignment and corotation of weak, TC-like vortices via linear vortex Rossby waves. *J. Atmos. Sci.*, **58**, 2306–2330, doi:[10.1175/1520-0469\(2001\)058<2306:TDAACO>2.0.CO;2](https://doi.org/10.1175/1520-0469(2001)058<2306:TDAACO>2.0.CO;2).
- , and —, 2015: Evaluation of a heuristic model for tropical cyclone resilience. *J. Atmos. Sci.*, **72**, 1765–1782, doi:[10.1175/JAS-D-14-0318.1](https://doi.org/10.1175/JAS-D-14-0318.1).
- , —, and L. D. Grasso, 2004: A new look at the problem of tropical cyclones in vertical shear flow: Vortex resiliency. *J. Atmos. Sci.*, **61**, 3–22, doi:[10.1175/1520-0469\(2004\)061<0003:ANLATP>2.0.CO;2](https://doi.org/10.1175/1520-0469(2004)061<0003:ANLATP>2.0.CO;2).
- , M. D. Eastin, and J. F. Gamache, 2009: Rapidly intensifying Hurricane Guillermo (1997). Part I: Low-wavenumber structure and evolution. *Mon. Wea. Rev.*, **137**, 603–631, doi:[10.1175/2008MWR2487.1](https://doi.org/10.1175/2008MWR2487.1).
- , R. F. Rogers, and S. Lorsolo, 2013: Environmental flow impacts on tropical cyclone structure diagnosed from airborne Doppler radar composites. *Mon. Wea. Rev.*, **141**, 2949–2969, doi:[10.1175/MWR-D-12-00334.1](https://doi.org/10.1175/MWR-D-12-00334.1).
- , J. F. Gamache, P. P. Dodge, and A. S. Goldstein, 2016: Evaluation of the NOAA Gulfstream-IV tail Doppler radar in tropical cyclones. *32nd Conf. on Hurricanes and Tropical Meteorology*, San Juan, Puerto Rico, Amer. Meteor. Soc., 11C.4., <https://ams.confex.com/ams/32Hurr/webprogram/Paper292919.html>.
- Reynolds, R. W., T. M. Smith, C. Liu, D. B. Chelton, K. S. Casey, and M. G. Schlax, 2007: Daily high-resolution-blended analyses for sea surface temperature. *J. Climate*, **20**, 5473–5496, doi:[10.1175/2007JCLI1824.1](https://doi.org/10.1175/2007JCLI1824.1).
- Riemer, M., and F. Laliberté, 2015: Secondary circulation of tropical cyclones in vertical wind shear: Lagrangian diagnostic and pathways of environmental interaction. *J. Atmos. Sci.*, **72**, 3517–3536, doi:[10.1175/JAS-D-14-0350.1](https://doi.org/10.1175/JAS-D-14-0350.1).
- , M. T. Montgomery, and M. E. Nicholls, 2010: A new paradigm for intensity modification of tropical cyclones: Thermodynamic impact of vertical wind shear on the inflow layer. *Atmos. Chem. Phys.*, **10**, 3163–3188, doi:[10.5194/acp-10-3163-2010](https://doi.org/10.5194/acp-10-3163-2010).
- , —, and —, 2013: Further examination of the thermodynamic modification of the inflow layer of tropical cyclones by vertical wind shear. *Atmos. Chem. Phys.*, **13**, 327–346, doi:[10.5194/acp-13-327-2013](https://doi.org/10.5194/acp-13-327-2013).
- Rios-Berrios, R., and R. Torn, 2017: Climatological analysis of tropical cyclone intensity changes under moderate vertical



- wind shear. *Mon. Wea. Rev.*, **145**, 1717–1738, doi:[10.1175/MWR-D-16-0350.1](https://doi.org/10.1175/MWR-D-16-0350.1).
- Rogers, R., P. Reasor, and S. Lorsolo, 2013: Airborne Doppler observations of the inner-core structural differences between intensifying and steady-state tropical cyclones. *Mon. Wea. Rev.*, **141**, 2970–2991, doi:[10.1175/MWR-D-12-00357.1](https://doi.org/10.1175/MWR-D-12-00357.1).
- , —, and J. A. Zhang, 2015: Multiscale structure and evolution of Hurricane Earl (2010) during rapid intensification. *Mon. Wea. Rev.*, **143**, 536–562, doi:[10.1175/MWR-D-14-00175.1](https://doi.org/10.1175/MWR-D-14-00175.1).
- , J. Zhang, J. Zawislak, H. Jiang, G. Alvey, E. Zipser, and S. Stevenson, 2016: Observations of the structure and evolution of Hurricane Edouard (2014) during intensity change. Part II: Kinematic structure and the distribution of deep convection. *Mon. Wea. Rev.*, **144**, 3355–3376, doi:[10.1175/MWR-D-16-0017.1](https://doi.org/10.1175/MWR-D-16-0017.1).
- Schecter, D. A., and M. T. Montgomery, 2007: Waves in a cloudy vortex. *J. Atmos. Sci.*, **64**, 314–337, doi:[10.1175/JAS3849.1](https://doi.org/10.1175/JAS3849.1).
- , —, and P. D. Reasor, 2002: A theory for the vertical alignment of a quasigeostrophic vortex. *J. Atmos. Sci.*, **59**, 150–168, doi:[10.1175/1520-0469\(2002\)059<0150:ATFTVA>2.0.CO;2](https://doi.org/10.1175/1520-0469(2002)059<0150:ATFTVA>2.0.CO;2).
- Schubert, W. H., and J. J. Hack, 1982: Inertial stability and tropical cyclone development. *J. Atmos. Sci.*, **39**, 1687–1697, doi:[10.1175/1520-0469\(1982\)039<1687:ISATCD>2.0.CO;2](https://doi.org/10.1175/1520-0469(1982)039<1687:ISATCD>2.0.CO;2).
- Simpson, R., and H. Riehl, 1958: Mid-tropospheric ventilation as a constraint on hurricane development and maintenance. Preprints, *Tech. Conf. on Hurricanes*, Miami Beach, FL, Amer. Meteor. Soc., D4-1–D4-10.
- Smith, R. K., and M. T. Montgomery, 2016: The efficiency of diabatic heating and tropical cyclone intensification. *Quart. J. Roy. Meteor. Soc.*, **142**, 2081–2086, doi:[10.1002/qj.2804](https://doi.org/10.1002/qj.2804).
- , J. A. Zhang, and M. T. Montgomery, 2017: The dynamics of intensification in a Hurricane Weather Research and Forecasting simulation of Hurricane Earl (2010). *Quart. J. Roy. Meteor. Soc.*, **143**, 293–308, doi:[10.1002/qj.2922](https://doi.org/10.1002/qj.2922).
- Stevenson, S. N., K. L. Corbosiero, and J. Molinari, 2014: The convective evolution and rapid intensification of Hurricane Earl (2010). *Mon. Wea. Rev.*, **142**, 4364–4380, doi:[10.1175/MWR-D-14-00078.1](https://doi.org/10.1175/MWR-D-14-00078.1).
- Tang, B., and K. Emanuel, 2010: Midlevel ventilation's constraint on tropical cyclone intensity. *J. Atmos. Sci.*, **67**, 1817–1830, doi:[10.1175/2010JAS3318.1](https://doi.org/10.1175/2010JAS3318.1).
- , and —, 2012: Sensitivity of tropical cyclone intensity to ventilation in an axisymmetric model. *J. Atmos. Sci.*, **69**, 2394–2413, doi:[10.1175/JAS-D-11-0232.1](https://doi.org/10.1175/JAS-D-11-0232.1).
- Tao, C., and H. Jiang, 2015: Distributions of shallow to very deep precipitation–convection in rapidly intensifying tropical cyclones. *J. Climate*, **28**, 8791–8824, doi:[10.1175/JCLI-D-14-00448.1](https://doi.org/10.1175/JCLI-D-14-00448.1).
- Tao, D., and F. Zhang, 2015: Effects of vertical wind shear on the predictability of tropical cyclones: Practical versus intrinsic limit. *J. Adv. Model. Earth Syst.*, **7**, 1534–1553, doi:[10.1002/2015MS000474](https://doi.org/10.1002/2015MS000474).
- Vigh, J. L., and W. H. Schubert, 2009: Rapid development of the tropical cyclone warm core. *J. Atmos. Sci.*, **66**, 3335–3350, doi:[10.1175/2009JAS3092.1](https://doi.org/10.1175/2009JAS3092.1).
- Willoughby, H. E., and M. B. Chelmon, 1982: Objective determination of hurricane tracks from aircraft observations. *Mon. Wea. Rev.*, **110**, 1298–1305, doi:[10.1175/1520-0493\(1982\)110<1298:ODOHTF>2.0.CO;2](https://doi.org/10.1175/1520-0493(1982)110<1298:ODOHTF>2.0.CO;2).
- , F. D. Marks, and R. J. Feinberg, 1984: Stationary and propagating convective bands in asymmetric hurricanes. *J. Atmos. Sci.*, **41**, 3189–3211, doi:[10.1175/1520-0469\(1984\)041<3189:SAMCBI>2.0.CO;2](https://doi.org/10.1175/1520-0469(1984)041<3189:SAMCBI>2.0.CO;2).
- Wu, L., S. A. Braun, J. Halverson, and G. Heymsfield, 2006: A numerical study of Hurricane Erin (2001). Part I: Model verification and storm evolutionary. *J. Atmos. Sci.*, **63**, 65–86, doi:[10.1175/JAS3597.1](https://doi.org/10.1175/JAS3597.1).
- Zagrodnik, J. P., and H. Jiang, 2014: Rainfall, convection, and latent heating distributions in rapidly intensifying tropical cyclones. *J. Atmos. Sci.*, **71**, 2789–2809, doi:[10.1175/JAS-D-13-0314.1](https://doi.org/10.1175/JAS-D-13-0314.1).
- Zawislak, J., H. Jiang, G. Alvey, E. Zipser, R. Rogers, J. Zhang, and S. Stevenson, 2016: Observations of the structure and evolution of Hurricane Edouard (2014) during intensity change. Part I: Relationship between the thermodynamic structure and precipitation. *Mon. Wea. Rev.*, **144**, 3333–3354, doi:[10.1175/MWR-D-16-0018.1](https://doi.org/10.1175/MWR-D-16-0018.1).
- Zhang, F., and D. Tao, 2013: Effects of vertical wind shear on the predictability of tropical cyclones. *J. Atmos. Sci.*, **70**, 975–983, doi:[10.1175/JAS-D-12-0133.1](https://doi.org/10.1175/JAS-D-12-0133.1).
- Zhang, J. A., R. F. Rogers, P. Reasor, E. Uhlhorn, and F. D. Marks Jr., 2013: Asymmetric hurricane boundary layer structure from dropsonde composites in relation to the environmental wind shear. *Mon. Wea. Rev.*, **141**, 3968–3984, doi:[10.1175/MWR-D-12-00335.1](https://doi.org/10.1175/MWR-D-12-00335.1).
- , J. J. Cione, E. A. Kalina, E. W. Uhlhorn, T. Hock, and J. A. Smith, 2017: Observations of infrared sea surface temperature and air–sea interaction in Hurricane Edouard (2014) using GPS dropsondes. *J. Atmos. Oceanic Technol.*, **34**, 1333–1349, doi:[10.1175/JTECH-D-16-0211.1](https://doi.org/10.1175/JTECH-D-16-0211.1).